A competition network connects Rab5 and Rab11 GTPases at the surface of endocytic structures

iScience

Article

A competition network connects Rab5 and Rab11 GTPases at the surface of endocytic structures

Graphical abstract

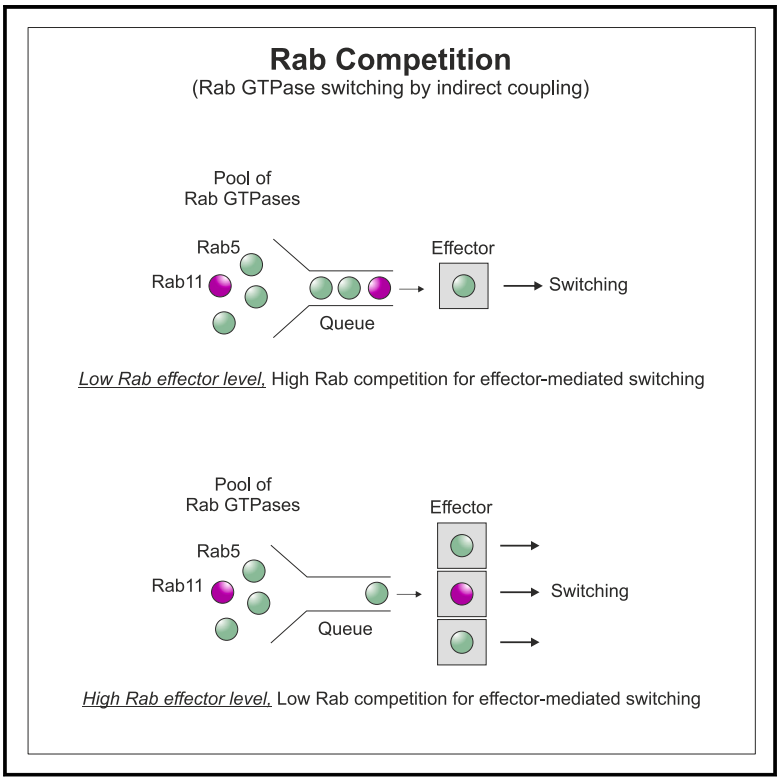

Highlights

- Rab GTPases regulate membrane trafficking via competitive effector binding
- Rab competition networks generate versatile crosstalk scheme in endocytic signaling
- Loop index links GTPase activation to abundance, revealing regulation patterns
- Zfyve26 influences Rab5 and Rab11 activation, with potential implications for SPG15 disease

Authors

Elsi Ferro, Simone Tealdi, Jean Piero Margaria, ..., Andrea Pagnani, Carla Bosia, Carlo Cosimo Campa

Correspondence

carla.bosia@polito.it (C.B.), carlocosimo.campa@iigm.it (C.C.C.)

In brief

Molecular interaction; Cell biology; Organizational aspects of cell biology; Functional aspects of cell biology

Ferro et al., 2025, iScience *28*, 112170
April 18, 2025
https://doi.org/10.1016/j.isci.2025.112170

CellPress

iScience

CellPress
OPEN ACCESS

Article

A competition network connects Rab5 and Rab11 GTPases at the surface of endocytic structures

Elsi Ferro,[1,2] Simone Tealdi,[2,3] Jean Piero Margaria,[4,5] Maria Chiara De Santis,[4] Luca Gozzelino,[2,6] Marta Cunial,[2] Chiara Enrico Bena,[1,8] Irene Franco,[5] Emilio Hirsch,[4] Andrea Gamba,[1,2,7] Andrea Pagnani,[1,2] Carla Bosia,[1,2,9,*] and Carlo Cosimo Campa[2,6,9,10,*]

[1]Department of Applied Science and Technology, Politecnico di Torino, Corso Duca degli Abruzzi 24, 10129 Turin, Italy
[2]Italian Institute for Genomic Medicine, SP142 km 3,95, 10060 Candiolo, Italy
[3]Department of Mechanical and Aerospace Engineering, Politecnico di Torino, Corso Duca degli Abruzzi 24, 10129 Turin, Italy
[4]Department of Molecular Biotechnology and Health Sciences, Molecular Biotechnology Center, University of Turin, Via Nizza 52, 10126 Turin, Italy
[5]Somatic Mutation Mechanisms Unit, Division of Genetics and Cell Biology, IRCCS Ospedale San Raffaele, Via Olgettina 58, 20132 Milan, Italy
[6]Candiolo Cancer Institute, FPO – IRCCS, SP142 km 3,95, 10060 Candiolo, Italy
[7]Istituto Nazionale di Fisica Nucleare (INFN), Via Pietro Giuria 1, 10125 Turin, Italy
[8]Present address Université Paris-Saclay, INRAE, AgroParisTech, Micalis Institute, Jouy-en-Josas 78350, France
[9]These authors contributed equally
[10]Lead contact
*Correspondence: carla.bosia@polito.it (C.B.), carlocosimo.campa@iigm.it (C.C.C.)
https://doi.org/10.1016/j.isci.2025.112170

SUMMARY

Specificity in membrane trafficking relies on the interaction between Rab small GTPase proteins and their molecular effectors. However, the evidence that different Rab proteins can bind to common effectors challenges this view. Here, we show that molecular competition between distinct Rab GTPases for a shared protein can link diverse membrane trafficking pathways. Theoretical analysis and experimental data support a role for Zfyve26 as a part of a competitive network that modulates changes in Rab5-Rab11 abundance, activation status, and correlation at the surface of single endocytic structures. By leveraging on the Loop index, a novel metric that couples the GTP-bound fraction and the total amount of Rab GTPase, we infer the saturation of Zfyve26 molecules at the endocytic surface from time-lapse imaging data. Our findings establish that transduction in the endocytic system is governed by stoichiometric constraints determining the trade-off between different trafficking pathways at the surface of a membrane-bound organelle.

INTRODUCTION

Rab small GTPases are molecular switches decorating organelle surfaces and involved in both organization and maturation of membranes along intracellular trafficking pathways.[1,2] To fulfill its function, each Rab must be localized to, and activated at, specific organelle sites.[3] GDP dissociation inhibitors (GDIs) promote Rabs cytosolic localization whereas guanine nucleotide exchange factors (GEFs) and GTPase-activating proteins (GAPs) are responsible for Rab's conversion either into the "on" (GTP-bound), or into the "off" (GDP-bound) state, respectively.[4] By interacting with guanine nucleotides, either GDP or GTP, Rabs can control different molecular effectors and, in turn, GEF and GAP proteins, thereby creating both regulatory loops (e.g., feedback and feedforward loops) and interconnected signaling cascades.[5–10]

To investigate potential mechanisms in Rab network regulation, extensive biochemical efforts have been focused on the characterization of Rab:effector interactions.[11,12] Both divalent Rab effectors, and effector-effector Rab interaction networks have been discovered, providing new insights into mechanism of trafficking specificity.[13–15] However, different Rabs can recognize, either directly or indirectly, the same effector, thus indicating that multivalency and promiscuity are general features of Rab effector architecture.[16] This, in turn, implies that different Rabs may compete for effector binding, raising the question of how this process can be studied in living cells, where the affinity, stoichiometry, and abundance of the interacting proteins are beyond the direct control of the investigator.

Computational analysis indicates that competition for a shared resource can introduce crosstalk between different elements (i.e., competitors) that make up a functional network, even without direct interactions. By sharing resources, few competitors can give rise to many different functional complexes, whose distribution depends on the abundance, affinity strength and stoichiometry of the components.[17] As a consequence, strategies able to probe competition in regulatory

networks are mainly based on perturbation of the shared resource, and the subsequent quantitation, through correlation analysis, of the resulting co-occurrent variations among the competitors.[18] However, the translation of this approach to living cells can be difficult as it requires prior knowledge of the biochemical system under investigation. For example, either the exchange of material entering and leaving the network (open system) or a fixed number of molecules constituting the system (closed system) may affect correlation data and its interpretation.[19] Whether the correlation analysis of perturbed Rab networks can be used to investigate functional interaction between Rabs and their binding partners in living cells remains to be determined.

Here, we propose the Rab competition network hypothesis to explain the multivalency and promiscuity found for Rab effectors. Using coarse-grained computational models to suggest new kinds of analysis and guide their interpretation,[20] we enumerated hypothetical circuits with two Rab nodes that can exhibit crosstalk by interacting with a shared effector and, subsequently, we compared the functional relationship emerging for the different network topologies, using correlation analysis. Using such computational examination as a guide, we developed imaging and statistical procedures aimed at monitoring the interplay between Rab5 and Rab11, two small GTPases that connect the degradative and recycling transport routes, even without a direct interaction.[2,14,21,22] Perturbation of the functional relationships between these two GTPases was achieved by expressing either Rab11FIP5, a Rab11-effector part of the FERARI Rab5-Rab11 recycling complex, or Zfyve26, an endocytic protein which associate with and controls the activation status of Rab5 and Rab11.[23,24] This combination of computational and experimental analysis leads to a more general understanding of the role played by the Rab interaction network, ultimately suggesting that competitive communication might link Rab5 and Rab11 GTPases at the surface of endocytic organelles.

RESULTS

In silico design of artificial Rab interaction networks

Rab effectors control both the switching and the crosstalk of Rab GTPases.[9,25,26] In addition, the evidence that Rab effectors can bind different GTPases suggests that Rabs can compete for effector binding.[11,12,16] Using computational modeling to suggest measurable quantities and guide their interpretation,[20] we designed and analyzed *in silico* artificial Rab regulatory circuits in which concerted switching and crosstalk of different Rab small GTPases rely on functional interaction, for a common effector, regardless of whether such interaction is direct or mediated through intervening proteins (i.e., indirect) (Figures 1A–1D). Note that this approach is intended to explore the properties arising from this potential, but hypothetical, mode of interaction, and therefore does not attempt to reflect any real Rab molecular system.

We developed a theoretical framework that is simple enough to limit the number of parameters, yet complex enough to explore novel modes of interaction of a hypothetical Rab GTPase network. We decided to explore two distinct theoretical Rab modules (RabX, RabY), each one comprising the factors that regulate the GTPase cycle (GEFs, GAPs), interconnected by a Rab effector regulatory node (E), that has the potential to alter both GTPase nucleotide binding status and crosstalk. For each GTPase, the circuit space under examination was defined by different combinations of 4 distinct regulatory circuits, such as positive/negative feedback loops (FBLs) and coherent/incoherent feedforward loops (FFLs), and 2 modes of functional interaction between GTPases, herein referred as Rab competition (Figure 1A, left panel) and Rab cascade (Figure 1A, right panel), thus resulting in a total of 32 architectures.

We implemented coarse-grained models in which the theoretical endosomal membrane is surrounded by a finite cytosolic pool of both RabX and RabY, which move from the cytosol to the membrane (Figure 1B, top panel). We limited the shuttling of Rab proteins between these compartments to the inactive, GDP-bound form, whereas, in line with previous reports, we restricted to the membrane the localization of the active GTP-bound form.[6,7,9] We decided to model the Rab^{GDP} membrane association and its extraction as binding/unbinding rates. Similarly, we represented the activities of factors that regulate the GTPase activation cycle, such as GEFs and GAPs, as GDP/GTP exchange or GTP hydrolysis rates, respectively (Figure 1B, top panel, Materials and methods).

In natural Rab GTPase activation circuits, interactions between Rabs, and their effectors connect distinct GTPases and/or exacerbate changes in their nucleotide binding status.[9,25,26] However, values of these parameters for many different GTPases are still unknown. Therefore, we conceived an artificial representation of the potential, yet hypothetical, role played by such Rab effectors that employs effective reaction-rate constants to reflect the functional roles played by Rab binding partners within a competitive network, regardless of whether their interaction with Rabs is direct or indirect. In our artificial network, links connecting a Rab regulatory node to the Rab modules increase the apparent affinities for GEF/GAP proteins and hence their basal reaction rates. This in turn, generates self-regulatory loops in which each Rab controls its own switching (Materials and methods). We implemented this self-regulation mechanism by designing both positive feedback loops (pFBLs) and coherent feedforward loops (cFFLs), that increase the rate of nucleotide exchange via the Rab effector-GEF interaction, each of which originated from either the GTP- or the GDP-loaded Rab, respectively (Figure 1B, middle dashed squares, Materials and methods). In parallel, we provided both negative feedback loops (nFBLs) and incoherent feedforward loops (iFFLs) in which the increased rate of hydrolysis is triggered by either GTP or GDP-loaded GTPase, respectively (Figure 1B, bottom dashed squares) (Materials and methods).

We enumerated all network topologies by combinatorically varying the possible regulatory links between the Rab effector and GTPases, thus resulting in 16 different topologies. Note that using this approach, the Rab effector is sequestered by one GTPases at the time, thereby resulting in Rab competition. In addition, to specifically evaluate properties arising from this mode of interaction, we also created 16 cascade circuits, where one GTPase monopolises the Rab shared effector to regulate

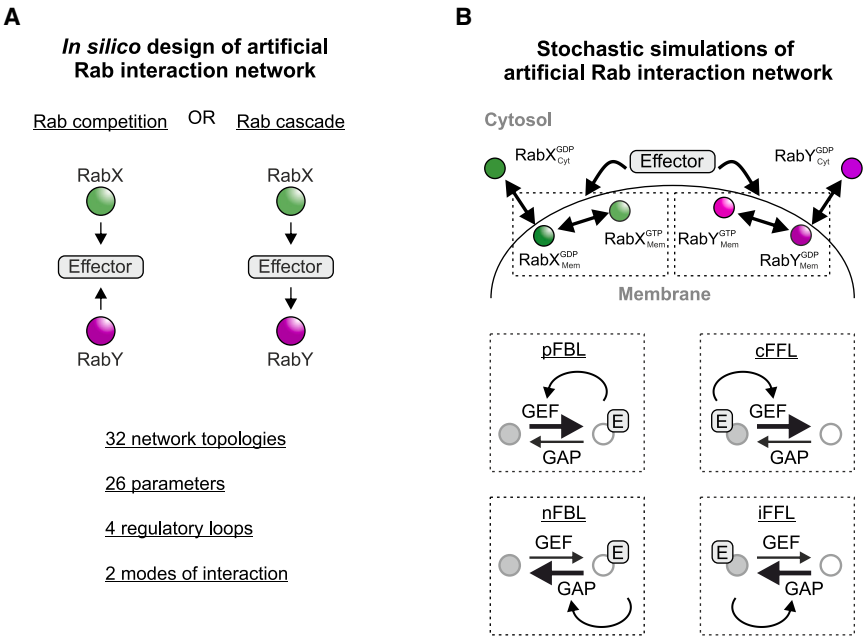

Figure 1. Design and analysis of artificial Rab interaction network by using a shared effector

(A) Schematic representation of competitive (left panel) and cascade (right panel) artificial functional interactions between distinct Rab activation modules (colored circles) characterized by a shared effector (gray square).

(B) Schematic representation of Rab shuttling from cytosol to endosomal membrane in the artificial Rab network (top panel). Schematic representation of self-regulatory loops used in this study (bottom panel). Gray and white circles represent either GDP or GTP-loaded Rabs, respectively. pFBL: positive feedback loop; nFBL: negative feedback loop; cFFL: coherent feedforward loop; iFFL: incoherent feedforward loop.

(C) Schematic representation of Pearson correlation analysis used for the characterization of artificial Rab network.

(D) Scoring of artificial Rab network based on correlation analysis as a function of Rab stoichiometry (Rabs ratio) and effector abundance (E = 50 and E = 400).

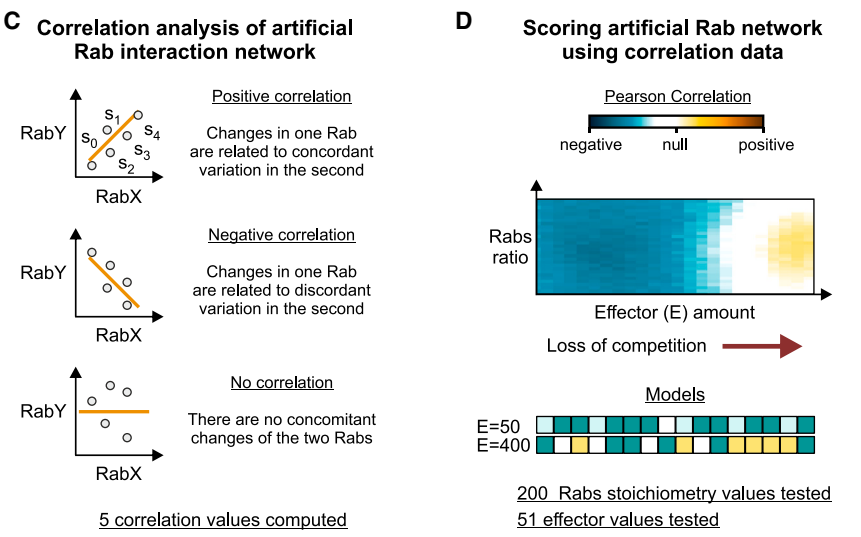

both its own biochemical activation and the activation of the other (Figure 2A, Materials and methods).

Correlation analysis of in silico artificial Rab interaction networks

To quantitatively describe our theoretical circuits, we performed correlation analysis of the 32 *in silico* designed artificial Rab interaction network. We used this statistical approach to express with a number (the Pearson coefficient) between −1 and +1 both the strength (the numerical value) and the direction (the sign) of the relationship between the variables that make up our theoretical network. We applied the correlation analysis to either active GTPases (Rab^{GTP}) or all membrane-bound ones, which can be active or inactive (Rab_{Mem}).

After each stochastic simulation reached the steady state, we calculated, for each network topology, the co-occurrent variations between the distinct GTPases species (i.e., GTP-bound, membrane-bound) using the Pearson correlation coefficient (Figure 1C). Positive and negative Pearson values distinguished co-occurrent interactions characterized by both parallel and opposite directions, respectively. On the contrary, uncoupling between molecular species resulted in null Pearson values (Figure 1C). Using this approach, we analyzed how the effector level changed the correlations by describing the coupling between: (1) the membrane-bound fraction of both RabX and RabY (i.e., $\rho(RabX_{Mem}, RabY_{Mem})$), (2) the GTP-bound fraction of both RabX and RabY (i.e., $\rho(RabX^{GTP}, RabY^{GTP})$), (3) the membrane-bound and GTP-bound fraction of either RabX or RabY herein referred to as "Loop Index" (i.e., $\rho(RabX_{Mem}, RabX^{GTP})$, $\rho(RabY_{Mem}, RabY^{GTP})$), as it allows to quantify, for the same GTPase, the coupling between its recruitment and its activation.

Next, we explored how distinct topologies performed upon variation of fundamental parameters controlling the reaction networks. Specifically, for each of the 32 different motifs, we explored 51 effector levels and 200 RabX/RabY stoichiometric values, and we visualized the correlation landscape as a heatmap in two-dimensional space (Figure 1D, top panel). The most meaningful differences in Pearson correlation were found

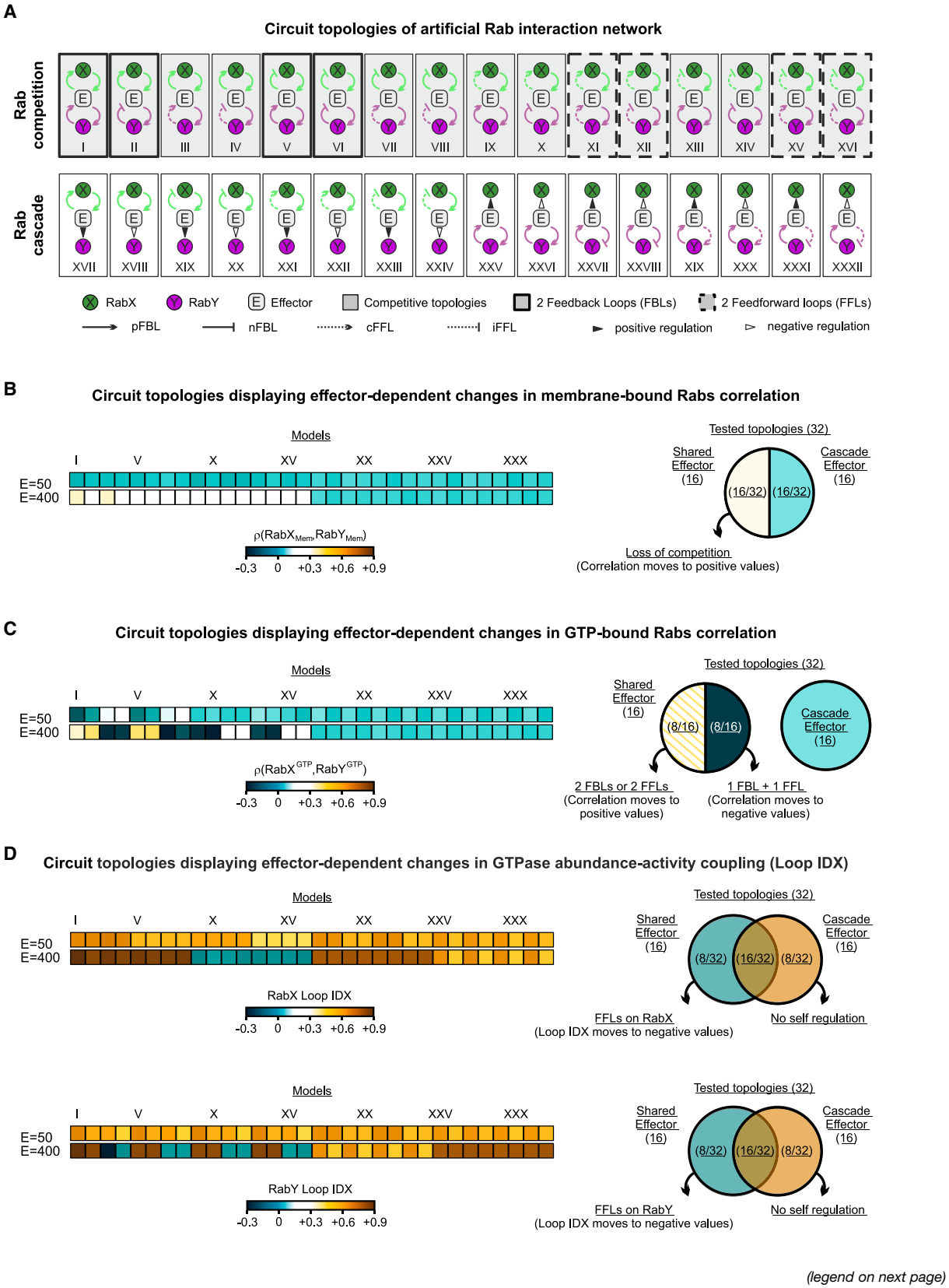

(legend on next page)

at E = 50 (number of molecules) and E = 400 (number of molecules) effector values in the presence of an equimolar amount of RabX and RabY (200 molecules each) (Figure 1D). To facilitate data visualization, Pearson values were displayed as pseudocolor squares (Figure 1D, bottom small panels). Next, we compared the Pearson value obtained at low effector amount of each network topology with the Pearson correlation resulting when the effector level is elevated. If the same mode of interaction (e.g., Rab competition, Rab cascade) or circuit motif (e.g., FBLs, FFLs) recurring in the 32 Rab interaction network showed similar Pearson coefficient changes between the low and high effector condition, then the Pearson analysis for this couple of variables was considered informative of the network topology. Conversely, if a motif failed to display consistent response to correlation analysis, we judged this couple of variables not indicative of the topology.

Identification of network topologies displaying Rab correlation changes

Within the complete set of 32 network topologies, 16 (50%) displayed higher correlation between membrane-bound RabX and RabY when effector abundance increased (Figures 2A and 2B). In terms of correlation changes, the performance of these 16 artificial Rab networks characterized by Rab competition for effector binding stood out above the basal (Pearson correlation value = −0.1) when the effector level increased (E = 400) and competition for the shared effector is loosened (Figure 2B, left panel, models I–XVI). This is in marked contrast to the lack of change in the Pearson coefficient for topologies with a Rab cascade interaction mode (Figure 2B, left, panel, models XVII–XXXII), in which changes in one element of the cascade affect the downstream but not the upstream element, and hence precluding co-occurrent variations of GTPases.

We hypothesized that some of the 32 network topologies might differ in Rab GTPase crosstalk, i.e., the mutual regulation of Rab nucleotide-binding states resulting from the intersection of their signaling pathways. Therefore, we compared the changes in Pearson correlation measured between GTP-bound RabX and RabY for each membrane topology at low and high effector level (Figure 2C). No differences were found for the 16 topologies with a Rab cascade interaction mode (Figure 2C, left panel, models XVII–XXXII). Conversely, within the 16 competitive topologies, 50% of them displayed an increase (Figure 2C, left panel, models I, II, V, VI, XI, XII, XV, and XVI), while the remaining showed a decrease, in the Pearson correlation value when the number of effector molecules increased (Figure 2C, left panel, models III, IV, VII, VIII, IX, X, XIII, and XIV).

We noted that when two FBLs are mixed—whether positive or negative—or when two FFLs are combined, the Pearson correlation went from negative to positive (Figure 2C, left panel, models I, II, V, VI, XI, XII, XV, and XVI). On the other hand, when one FBL and one FFL are combined, the Pearson correlation decreases (Figure 2C, left panel, models I, II, V, VI, XI, XII, XV, and XVI). This indicates that the mixture, rather than the type (i.e., FBLs, FFLs) of such self-regulatory circuits, determines the differential crosstalk between the theoretical Rabs.

To evaluate functional differences between self-regulatory motifs and topologies that contained such motif combinations, we calculated for each GTPase the Loop Index (IDX), a Pearson correlation estimate of the fluctuations between the membrane-bound and the GTP-bound Rab fraction (e.g., $\rho(RabX_{Mem}, RabX^{GTP})$). Within the 32 different topologies, 24 (75%) displayed changes in Loop IDX when the Effector level increased. Of them, only 8 (25%) showed a reduction (i.e., from positive to negative values) (Figure 2D, top right and bottom right panels).

We noted that motifs showing lower Loop IDX values corresponded to FFLs assembled in competitive topologies (Figure 2D, top left panel models IX–XVI, bottom left panel models III, IV, VII, VIII, XI, XII, XV, and XVI). In contrast, higher Loop IDX values were reached by increasing the effector amount in competitive networks containing FBLs, either positive or negative (Figure 2D, top left panel, models I–VIII, XVII–XXIV; bottom left panel, models I, II, V, VI, IX, X, XIII, XIV, XXV–XXXII).

Intuitively, FBLs with an excess of effector molecules showed positive Loop IDX since GTP-bound Rabs associated with effector molecules are less efficiently extracted from the membrane and not a suitable substrate for nucleotide exchange or GTP hydrolysis. This is shown by representative activation and abundance curves obtained for increasing amount of Rab effector and Rab ratio in both competitive and cascade Rab models (models I–IV and XVII, Figures S1, S2A–S2E, S3–S5A, S5B, and S5D). Such diminished membrane extraction also occurred with FFLs but, differently to FBLs, resulted in negative Pearson correlation when the Rab effector amount increased and in contrast to the cascade model (models I-IV, XVII, Figures S3–S5C and S5E). Thus, the excess of effector molecules blocked the GDP-bound GTPase in the membrane, thereby preventing both nucleotide exchanges and Rab membrane extraction. Consistently, for all the 32 models, variation of both effector levels and RabX/RabY stoichiometry values

Figure 2. Correlation analysis of artificial Rab interaction network

(A) Schematic representation of circuit topologies of artificial Rab interaction network.

(B) Pearson correlation quantification between membrane-bound RabX and RabY at low (E = 50) and high (E = 400) effector level for the 32 distinct artificial network topologies (left panel). Representation of artificial network topologies sharing similar Pearson correlation coefficient changes as a function of effector level variation (right panel).

(C) Pearson correlation quantification between GTP-bound RabX and RabY at low (E = 50) and high (E = 400) effector level for the 32 distinct artificial network topologies (left panel). Representation of artificial network topologies sharing similar Pearson correlation coefficient changes as a function of effector level variation (right panel).

(D) Quantification of Loop index (IDX) between the membrane-bound and the GTP-bound RabX fraction at low (E = 50) and high (E = 400) effector level for the 32 distinct artificial network topologies (top, left panel). Representation of artificial network topologies sharing similar Pearson correlation coefficient changes as a function of effector level variation (top, right panel). Quantification of Loop index (IDX) between the membrane-bound and the GTP-bound RabY fraction at low (E = 50) and high (E = 400) effector level for the 32 distinct artificial network topologies (bottom, right panel). Representation of artificial network topologies sharing similar Pearson correlation coefficient changes as a function of effector level variation (bottom, right panel).

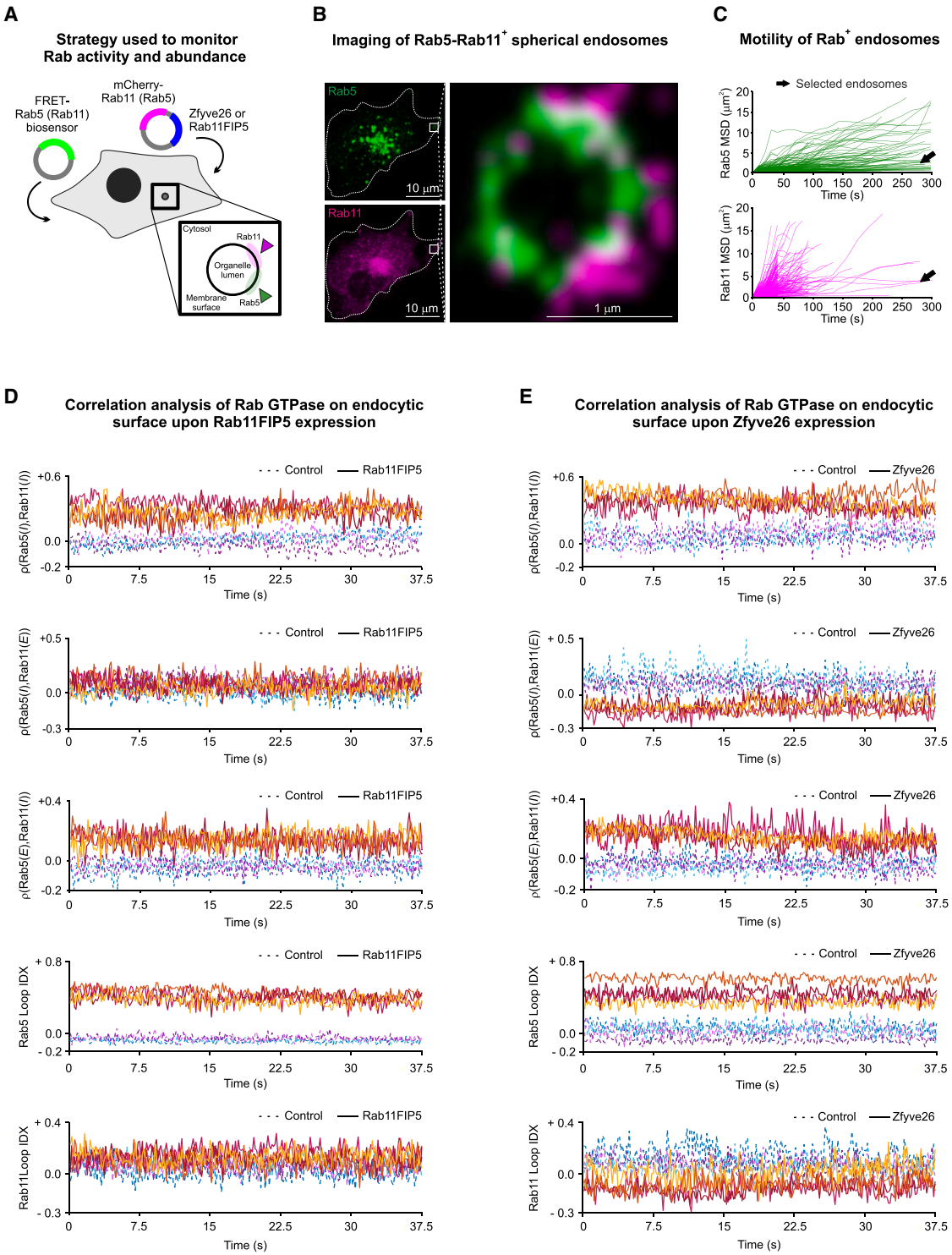

Figure 3. Measure of Rab5 and Rab11 functional interactions using FRET imaging and correlation analysis

(A) Schematic representation of the imaging procedure employed to measure Rab5 and Rab11 functional interaction using Rab5 and Rab11 fluorescent probes and activity sensors. The square box represents the magnification of schematic spherical endosomes with Rab5 and Rab11 fluorescent tagged proteins.

(B) Representative localization images of both Rab5 FRET biosensor (green) and mCherry-Rab11 (magenta) in the same single Cos-7 cell. Scale bars for whole cell (left panel) and the enlarged spherical endosome (right panel) are shown.

(C) Quantification of both Rab5-positive (top panel) and Rab11-positive (bottom panel) structures motility in Cos-7 cells (mean square displacement, MSD). *n* = 198 Rab5-positive structures ans *n* = 322 Rab11-positive structures. Black arrow indicates static structures used for subsequent analysis.

(legend continued on next page)

did not result in significant changes in correlation estimates including Loop IDX values, thus confirming the centrality of the type of self-regulatory motif in the Loop IDX estimates (Figures S1–S5F, models I–IV, XVII).

Our analysis showed that networks with competitive topology generate co-occurrent variations in Rab GTPases abundance and GTPase cross-talk that can be studied using correlation analysis. Increasing the effector level reduces competition for the shared resource, resulting in distinct correlation profiles that can be identified using the Loop IDX.

Probing Rab5 and Rab11 functional interactions using FRET imaging and correlation analysis

Our computational analysis defined a landscape of Rab interaction networks generated by potential, yet hypothetical, Rab effectors and provided guidance on how to interpret correlation data arising from different functional interactions. This led us to employ this statistical approach to probe Rab functional interactions in living cells. By using genetically encoded Rab FRET biosensors, we quantified both abundance and activation status of GTPases, key elements in our correlation analysis.

We chose the endocytic trafficking regulators Rab5 and Rab11 as GTPases of interest because of the availability of genetically encoded FRET biosensor versions, namely Raichu-Rab5 and As-Rab11, respectively.[27,28] Although efficient, these biosensors consist of similar FRET pairs (cyan and yellow fluorescent proteins) causing spectral crosstalk. Consequently, we limited our imaging analysis to one GTPase at a time. By co-expressing Raichu-Rab5 together with mCherry-Rab11a we monitored both activation status and abundance of Rab5 and, in parallel, Rab11 levels (Figure 3A). Subsequently, in order to obtain the missing information about Rab11 activation status, we performed similar experiments in cells expressing the As-Rab11 biosensor and mCherry-Rab5a.

Time-lapse analysis revealed fast movement of both Raichu-Rab5 and mCherry-Rab11a positive structures during the continuous uptake of transferrin (Tf), a recycling ligand that we have previously found to induce Rab11 switching on periplasmalemmal endocytic structures[28] (Figures 3B and 3C). These labeled membranes were observed to detach and collapse, producing a bundle of structures distributed throughout the cytosol (Figure S6A). Although these structures might derive from concerted Rab function during trafficking process, both their irregular shape and their rapid movement made them unsuitable for our FRET-based imaging strategy (Figure 3C). Nonetheless, during the experimentation, we found the occurrence of endocytic structures characterized by a nearly perfect spherical geometry with higher dimension (~1 μm diameter), slower motility and positivity for both Raichu-Rab5 and mCherry-Rab11a, thus providing a suitable model for our study (Figure 3B). These structures were not artifactual, since they occurred in physiological conditions as demonstrated by immunostaining of endogenous Rab5 and Rab11 (Figure S6B). We found that a minor portion corresponding to the ~0.15% of both Rab5 and Rab11 positive structures labeled such circular compartments (Figure S6C). Coherently, these spherical endosomes were rare and only 15% of the cells showed at least one of them, with an average of ~1.6 circular endosomes per positive cell (Figure S6D). Note that the frequency of these structures can be increased, but only in certain cell types, as suggested by the comparison of the fibroblast-like and glioma cell lines treated with transferrin (Figures S6C and S6D).

Using these spherical endosomes as a case study, we explored the functional interaction between Rab5 and Rab11, by monitoring both their activation status (i.e., FRET efficiency (*E*)) and their abundance (i.e., fluorescence intensity (*I*)). We acquired time-lapse FRET images on the bidimensional focal plane for at least ~30 s of periplasmalemmal organelles decorated by Raichu-Rab5 and tagged mCherry-Rab11a with a 3:1 relative stoichiometry (Rab5/Rab11 ratio = 2.93; p value = 0.001, Materials and methods). In addition, to ensure a complete reconstruction of the original endocytic signal in space and time according to the Nyquist criterion, we sampled submicron-sized pixels (~50 nm) at a high temporal rate (~150 ms) and coherently with the rapid temporal scale of GTPase signaling changes (Materials and methods).[28] Next, for every time frame, we computed three distinct Pearson correlation coefficients (ρ), derived from our theoretical observation, and resulting from the association between fluorescence intensity (*I*) and FRET efficiency (*E*) (Materials and methods). Specifically, we calculated the coupling between (1) membrane abundance of both Rab5 and Rab11 ($\rho(Rab5(I), Rab11(I))$), (2) Rab5 (or Rab11) activation status and Rab11 (or Rab5) membrane abundance ($\rho(Rab5(E), Rab11(I))$, $\rho(Rab5(I), Rab11(E))$), (3) Rab5 (or Rab11) abundance and activation status, i.e., the Loop IDX ($\rho(Rab5(I), Rab5(E))$, $\rho(Rab11(I), Rab11(E))$). Lastly, we perturbed the Rab5-Rab11 network by expressing, together with the mCherry-tagged GTPases, either Rab11FIP5 or Zfyve26, two distinct Rab effectors.[23,24]

Fluctuations resulted from temporal profiles of correlation data with constant mean level, thus supporting value averaging to summarize each dataset (Figures 3D and 3E; Table 1). We observed that Rab11FIP5/Zfyve26 expression increased $\rho(Rab5(I), Rab11(I))$, indicating a role for these proteins in regulating the abundance of both Rab5 and Rab11 at the surface of endocytic structures. Additionally, the co-occurrence of

(D) Representative correlation profiles computed for different combinations of both Rab5 and Rab11 fluorescence intensity (I) and FRET efficiency (E) values measured at the surface of a single spherical endosomes. Dashed and solid lines represent control and Rab11FIP5 expressing cells, respectively (4 trajectories per condition are displayed). n = 12 endosomes for cells co-transfected with Rab5 FRET biosensor, mCherry-Rab11 and either control or Rab11FIP5 plasmids. n = 13 endosomes for cells co-transfected with Rab11 FRET biosensor, mCherry-Rab5 and control plasmid; n = 11 endosomes for cells co-transfected with Rab11 FRET biosensor, mCherry-Rab5 and Rab11FIP5.

(E) Representative correlation profiles computed for different combinations of both Rab5 and Rab11 fluorescence intensity (I) and FRET efficiency (E) values measured at the surface of a single spherical endosomes. Dashed and solid lines represent control and Zfyve26 expressing cells, respectively (4 trajectories per condition are displayed). n = 16 endosomes for cells co-transfected with Rab5 FRET biosensor, mCherry-Rab11 and either control or Zfyve26 plasmids. n = 8 endosomes for cells co-transfected with Rab11 FRET biosensor, mCherry-Rab5 and control plasmid. n = 9 endosomes for cells co-transfected with Rab11 FRET biosensor, mCherry-Rab5 and Zfyve26 plasmids.

Table 1. Quantification of Pearson correlations of Rab5 and Rab11 GTPases at the surface of a single endosome

	ρ Rab5(*I*),Rab11(*I*)	ρ Rab5(*I*),Rab11(*E*)	ρ Rab5(*E*),Rab11(*I*)	Rab5 Loop IDX	Rab11 Loop IDX
Control	+0.10 (±0.04; *n* = 12)	+0.06 (±0.02; *n* = 13)	−0.05 (±0.03; *n* = 12)	+0.02 (±0.03; *n* = 12)	+0.08 (±0.03; *n* = 13)
Rab11FIP5	+0.45 (±0.07; *n* = 12; p<***)	+0.08 (±0.02; *n* = 11; ns)	+0.22 (±0.04; *n* = 12; p<***)	+0.42 (±0.04; *n* = 12; p<***)	+0.14 (±0.02; *n* = 11; ns)
Control	+0.11 (±0.04; *n* = 16)	+0.07 (±0.01; *n* = 8)	−0.05 (±0.02; *n* = 16)	+0. 01 (±0.03; *n* = 16)	+0.11 (±0.03; *n* = 8)
Zfyve26	+0.29 (±0.07; *n* = 16; p<*)	−0.06 (±0.02; *n* = 9; p<***)	+0.17 (±0.03; *n* = 16; p<***)	+0.43 (±0.04; *n* = 16; p<***)	+0.02 (±0.04; *n* = 9; ns)

Quantification of Pearson correlation coefficient between abundance (I, arbitrary units) and FRET efficiency (E, arbitrary units) of both Rab5 and Rab11 GTPases in control and Zfyve26 expressing cells. Numbers between brackets indicate: S.E.M the standard error, number of endosomes analyzed, and the *p* value obtained by two-sample t test between control and Rab11FIP5/Zfyve26 tested conditions, respectively. ns, not significant, * *p* value <0.05, *** *p* value <0.001.

changes in GTPase levels suggests a functional link between Rab5 and Rab11. Furthermore, these data, when interpreted within the context of our theoretical analysis (Figure 2B), allowed us to speculate about competing interactions that might occur within the Rab5-Rab11 network.

To better characterize the Rab5-Rab11 functional interaction, we quantified the coupling between GTP-bound Rab5 and Rab11 abundance (ρ *Rab*5(*E*),*Rab*11(*I*)) as well as the co-occurrent variation between Rab5 abundance and GTP-bound Rab11 (ρ *Rab*5(*I*), *Rab*11(*E*)) in cells expressing either Rab11FIP5 or Zfyve26. Expression of Rab11FIP5 shifted both Pearson correlations to more positive values, whereas expression of Zfyve26 gave the opposite result, higher for GTP-bound Rab5 and Rab11 abundance and lower for Rab5 abundance and GTP-bound Rab11 (Figures 3D and 3E). In order to interpret this measurement, we decided to include in our theoretical analysis the calculation of the Pearson correlation estimate between GTP-bound RabX and RabY membrane fractions (e.g., $\rho(RabX^{GTP}, RabY_{Mem})$), as well as the co-occurrent variation between RabX membrane-bound and the GTP-bound RabY fractions (e.g., $\rho(RabX_{Mem}, RabY^{GTP})$ (Figures S7A and S7B) since our theoretical data were limited to the characterization of Pearson correlation resulting from the comparison of Rab GTP-bound fraction only (Figure 2C). In this way, we found that in competitive network topologies, an increase in Pearson's correlation implied FBLs acting on the GTP-bound Rab variable ($RabX^{GTP}$, $RabY^{GTP}$). Conversely, a switch to negative correlation values characterized FFLs on the GTP-bound Rab variable ($RabX^{GTP}$, $RabY^{GTP}$). This suggests a relationship between the abundance and activation status of the two different GTPase (Figure S7A, models I-VIII).

Next, we quantified the Rab5 Loop IDX, i.e., the co-occurrent variation in GTP-bound Rab5 and its abundance, in cells expressing either Rab11FIP5 or Zfyve26 (Figures 3D and 3E). For both conditions, correlation moved to higher Pearson values, suggesting a functional role of these effectors in mediating functional coupling in Rab5 GTPase activation (Figures 3D and 3E). Conversely, opposite results were obtained when analyzing the Rab11 Loop IDX in cells expressing either Rab11FIP5 or Zfyve26 (Figures 3D and 3E). In particular, Rab11FIP5 prompted Pearson correlation to higher values while Zfyve26 expression induced Pearson reduction toward more negative values (Figures 3D and 3E). Comparison of these data with theoretical analysis allowed us to speculate about functional differences between self-regulatory motifs and network topologies that contained such motif combinations. As an example, we might associate the measured positive Rab5 and Rab11 Loop IDXs found in Rab11FIP5 cells to circuits composed by two FBLs, either positive or negative, one for each GTPase (Figure 2A models I, II, V, VI). In contrast, the positive Rab5 and negative Rab11 Loop IDXs found after Zfyve26 expression might be interpreted as a Rab5-Rab11 competitive network composed by a Rab5 FBL and a Rab11 FFL (Figure 2A models III, IV, VII, VIII).

Our correlation analysis described the biological effect of different Rab effectors at the surface of a single endocytic structure and suggests a functional interaction between Rab5 and Rab11. In addition, the finding that Rab5 and Rab11 Loop IDXs moved in opposite directions in cells expressing elevated Zfyve26 levels pointed us to investigate in more detail this enigmatic Rab effector.

Validation of Zfyve26's role in Rab5-Rab11 functional interaction

Our correlation analysis indicated that Zfyve26 expression is associated to changes in abundance/activation status of both Rab5 and Rab11. To test the functional relevance of our statistical approach, we performed immunofluorescence microscopy on both GTPases (Figure 4A).

Imaging analysis showed that Zfyve26 expression reduced the number of Rab5 structures (Figure 4B). Similar effect was observed for Rab11 labeled endosomes (Figure 4B). In parallel, the amount of both GTPases at the endocytic surface increased, with minor changes in their dimension, thus suggesting altered association/dissociation of Rabs from membranes (Figures 4C and 4D). In addition, the evidence that the separation between the Rab5 and Rab11 domains decreased upon overexpression of Zfyve26 (Figures 4E and S11), a condition in which the number of potential Rab binding sites on the membrane could be increased, suggests a role for Rab competition in spatial regulation and compartmentalization of small GTPases.

Next, we evaluated the activation changes of Rab proteins using Rab pull-down activation assay (Figures 4F–4I). Expression of Zfyve26 lead to 1.5-fold increase and a 0.5-fold reduction in the content of endogenous GTP-bound Rab5 and GTP-bound Rab11, respectively (Figures 4F and 4H). Consistently, by using

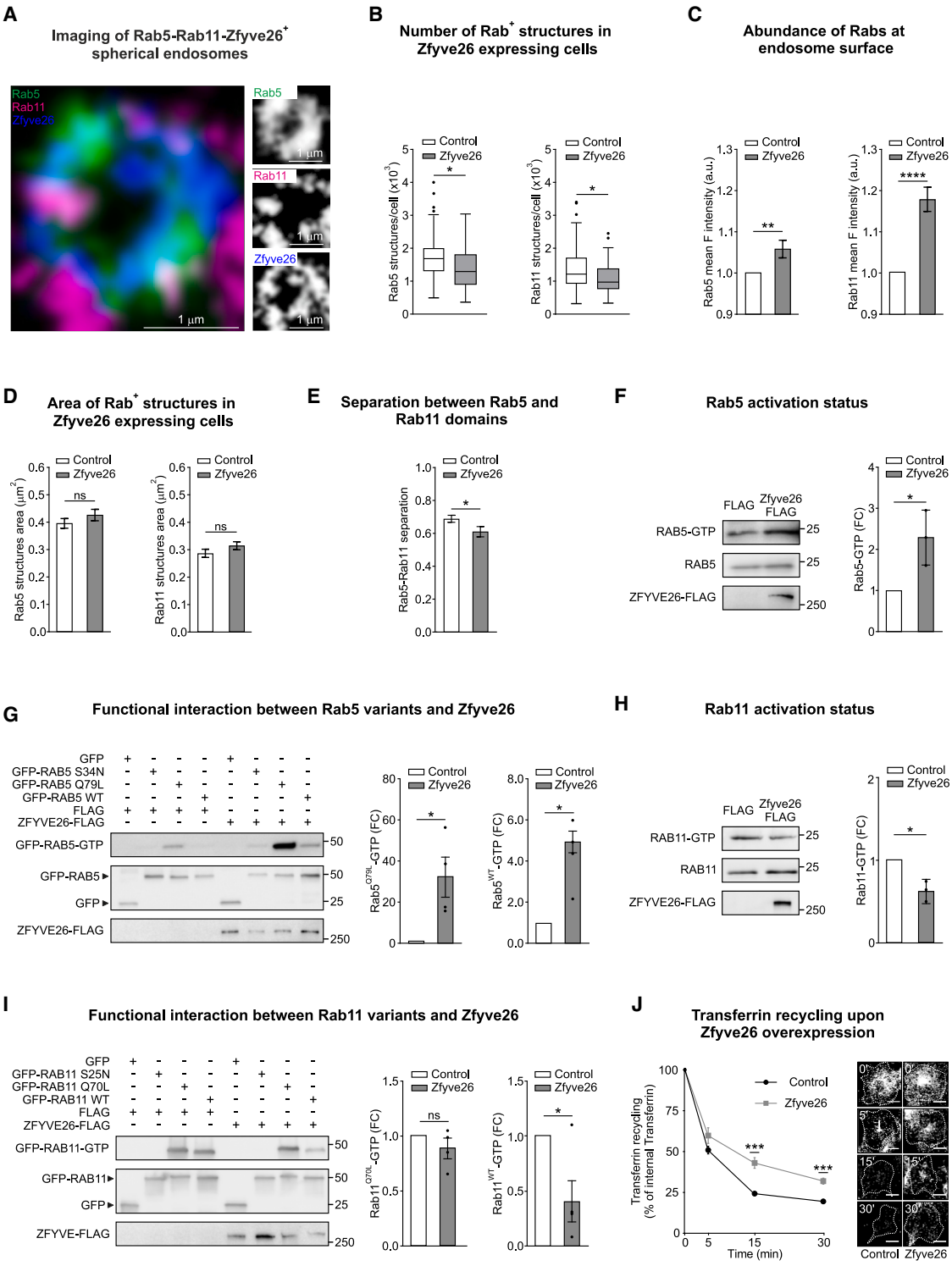

Figure 4. Functional impact of Zfyve26 on endogenous Rab5 and Rab11

(A) Representative images of spherical endosomes stained for endogenous Rab5 (green), endogenous Rab11 (magenta) and GFP-Zfyve26 (blue). Scale bars for merged image (left panel) and single channels (right panels) are displayed.

(B) Number of Rab5 (left panel) and Rab11 (right panel) structures per single cell. Boxplots indicate median (middle line), 25th, 75th percentile (box) and 5th and 95th percentile (whiskers) as well as outliers (single points). * p value <0.05 (Kolmogorov-Smirnov test), n = 102 cells in GFP expressing condition (control), n = 97 cells in GFP-Zfyve26 expressing condition (Zfyve26).

(legend continued on next page)

both Rab5 and Rab11 genetically encoded biosensors, we found similar changes in GTP-bound Rabs at the surface of the endocytic vesicle, thus strengthening the idea that the increased level of Zfyve26 controls Rab5 and Rab11 functional interaction through changes in their activation cycle (Table 2). To assess whether this effect might be caused by Rab self-regulation, we leveraged the ability of mutant Rab proteins to be locked in the GTP active form but still able to be loaded by GTP (e.g., $Rab5^{Q79L}$, $Rab11^{Q70L}$).[29] Cells expressing the GTPase deficient form of Rab5 triggered a 35-fold increase in Rab5 GTP content, thus suggesting positive feedback from GTP-bound Rab5 to itself (Figure 4G). Conversely, no difference was found by expressing Zfyve26 together with the GTPase deficient Rab11 mutant, thus indicating that feedback loops are not the Rab11 self-regulatory mode when Zfyve26 is elevated (Figure 4I). The increased accumulation of both Rab5 and Rab11 on the endocytic surface, their mixing and the fact that their nucleotide binding status is controlled in opposite direction by Zfyve26 implies dysfunctional endocytic recycling. Consistently, we measured delayed transferrin recycling in cells expressing Zfyve26 (Figure 4J).

Overall, these data indicate that Zfyve26 controls Rab5 and Rab11 functional interaction through changes in their activation status and their accumulation on the membrane, thereby suggesting that recruitment of Zfyve26 at the surface is relevant for tight control of Rab5 and Rab11 networks.

Identification of molecular cues controlling Zfyve26 level at the endocytic surface

Our data showed that changes in Zfyve26 levels play a pivotal role in the control of Rab5-Rab11 interaction. To investigate whether Zfyve26 abundance is regulated at the endocytic surface, we performed a fluorescence recovery after photo bleaching (FRAP) experiment using a GFP-tagged Zfyve26 version (Figure 5A). GFP-tagged Zfyve26 displayed a diffuse staining in the cytoplasm and accumulated on spherical endosomes. By recording the recovery rate of the fluorescent signal after photobleaching, we found that the fluorescence plateau level was lower than the pre-bleach intensity. This occurs because some of the FRAP-bleached molecules, nearly 20%, were slower diffusing/not dissociating from the membrane, thereby not participating in the recovery. Conversely, 80% of the molecules on organelle surface were recruited from the cytosol, thus demonstrating direct shuttling from the cytosol toward the endosome membrane (Figure 5A).

Next, in order to assess the mechanism that controls the recruitment of Zfyve26 to Rab5-Rab11 positive endosomes, we performed a Zfyve26 pull-down binding experiment using recombinant Rab proteins as probes. Zfyve26 interacted with both Rab5 and Rab11 in a nucleotide dependent manner, showing higher affinity for the Rab5 GTP-bound form and the Rab11 GDP-bound form, respectively (Figure 5B). Differently from other effectors, for which Rab molecules are sufficient for their recruitment,[15] Zfyve26 localization on endosomes did not seem related to the presence of Rab molecules, as demonstrated by the low overlap among Zfyve26, Rab5, Rab11 and membrane recruitment of GTPases (Figures 4A, S8A, and S8B). Therefore, searching for molecules able to induce an active recruitment of Zfyve26 on the membrane surface, we evaluated the role of the phosphatidylinositol 3-phosphate (PI(3)P), a membrane lipid interacting with Zfyve26.[30] We found that endosomal PI(3)P accumulation was triggered by transferrin stimulation (Figures S8C and S8D) and that acute pharmacological inhibition (1.5 h) of the lipid kinase PIK3C3, through the VPS34-IN1 inhibitor, promoted 20% reduction of PI(3)P structures and a concomitant 30% decrease of their PI(3)P content (Figure S8E). Using this pharmacological approach, we found that PI(3)P reduction was sufficient to induce the complete dispersion of Zfyve26 from membranes, a phenotype that was not rescued by either GTP/GDP Rab5 mutant forms (Figures 5C and 5D).

These data showed that Zfyve26 can shuttle from the membrane to the cytosol and that its membrane recruitment is

(C) Quantification of Rab5 (left panel) and Rab11 mean intensity (right panel) per single spherical endosome. Error bars indicate mean ± S.E.M. ** p value <0.01, **** p value <0.0001 (Student's t test), n = 26 spherical endosomes in GFP expressing condition (control) and n = 22 spherical endosomes GFP-Zfyve26 expressing condition (Zfyve26).

(D) Quantification of Rab5 (left panel) and Rab11 structures area (right panel) per single spherical endosomes. Error bars indicate mean ± S.E.M. ns = not significant, n = 26 spherical endosomes in GFP expressing condition (Control) and n = 22 spherical endosomes in GFP-Zfyve26 expressing condition (Zfyve26).

(E) Quantification of Rab5-Rab11 separation per single spherical endosome. Rab5-Rab11 separation is computed as 1 minus Rab5-Rab11 Mander's coefficient. Error bars indicate mean ± S.E.M. * p value <0.05 (Student's t test), n = 26 spherical endosomes in GFP expressing condition (Control) and n = 22 spherical endosomes in GFP-Zfyve26 expressing condition (Zfyve26).

(F) Quantification of endogenous Rab5-GTP content in cells upon Zfyve26 expression by using Rab5 activation pull-down assay. Representative western blot images (left panel) and quantification (right panel). FC indicate fold-change over control. Error bars indicate mean ± S.E.M. * p value <0.05 (Student's t test), n = 3 independent experiments.

(G) Quantification of transfected Rab5-GTP content in cells upon expression of Rab5 variants and/or Zfyve26 by using Rab5 activation pull-down assay. Representative western blot images (left panel) and quantification (right panels). FC indicate fold-change over control. Error bars indicate mean ± S.E.M. * p value <0.05 (Student's t test), n = 4 independent experiments.

(H) Quantification of endogenous Rab11-GTP content in cells upon Zfyve26 expression by using Rab11 activation pull-down assay. Representative western blot images (left panel) and quantification (right panel). FC indicate fold-change over control. Error bars indicate mean ± S.E.M. * p value <0.05 (Student's t test), n = 3 independent experiments.

(I) Quantification of transfected Rab11-GTP content in cells upon expression of Rab11 variants and/or Zfyve26 by using Rab11 activation pull-down assay. Representative western blot images (left panel) and quantification (right panels). FC indicates fold-change over control. Error bars indicate mean ± S.E.M. ns = not significant, * p value <0.05 (Student's t test), n = 4 independent experiments.

(J) Quantification of transferrin recycling using Alexa Fluor 647-conjugated human transferrin upon GFP (control) or GFP-Zfyve26 overexpression. Representative images (left panels) and quantification (right panel) (scale bar, 10 μm). Data represents mean ± S.E.M., *** p value <0.001 (Student's t test), n = 3 independent experiments.

Table 2. Quantification of both abundance and activity of Rab5 and Rab11 GTPases at the surface of a single endosome

	Rab5(*I*)	*Rab5*(*E*)	*Rab11*(*I*)	*Rab11*(*E*)
Control	30.2 (±6.85; *n* = 12)	0.22 (±0.02; *n* = 12)	38.18 (±4.16; *n* = 12)	0.48 (±0.03; *n* = 12)
Rab11FIP5	72.68 (±7.96; *n* = 12; p<***)	0.34 (±0.05; *n* = 12; p<*)	59.55 (±3.97; *n* = 12; p<**)	0.24 (±0.01; *n* = 12; p<***)
Control	32.90 (±7.22; *n* = 16)	0.24 (±0.03; *n* = 8)	43.93 (±7.35; *n* = 16)	0.46 (±0.04; *n* = 16)
Zfyve26	+77.70 (±7.09; *n* = 16; p<***)	0.40 (±0.02; *n* = 9; p<***)	48.40 (±5.87; *n* = 16; ns)	0.12 (±0.02; *n* = 16; p<***)

Quantification of mean abundance (I, arbitrary units) and FRET efficiency (E, arbitrary units) of both Rab5 and Rab11 GTPases in control and Zfyve26 expressing cells. Numbers between brackets indicate: S.E.M the standard error, number of endosomes analyzed, and the *p* value obtained by two-sample t test between control and Rab11FIP5/Zfyve26 tested conditions, respectively. ns, not significant, * *p* value <0.05, ** *p* value <0.01, *** *p* value <0.001.

controlled by PI(3)P, a lipid that accumulates during cargo internalization.

Probing Zfyve26 saturation at the endocytic surface using the loop Index

Our results indicate that Zfyve26 shuttles from cytosol to endosomes, leading to protein accumulation at the endocytic surface. Hence, we posit that these structures, which may contain the maximum number of Zfyve26 molecules, may experience biochemical saturation, a state where, proteins involved in the Rab activation reaction (e.g., Zfyve26) are operating at their maximum capacity, so adding more protein (e.g., Zfyve26) doesn't speed up the reaction.[31,32] From a statistical point of view this phenomenon is characterized by reduced fluctuations and coupling among molecular species and hence reduced Pearson correlation values.[18,19] Under these premises, we hypothesized that correlation analysis might be used to explore Rab effector saturation at the endocytic surface.

Given the ability of Loop IDX to assess the impact of Rab effectors on GTPase self-regulation, we hypothesized that changes in Loop IDX might reflect the onset of Zfyve26 saturation. Hence, we adapted our analytical approach to capture fluctuations of Loop IDX values at the surface of an endocytic vesicle. We sampled the segmented endosome corona of cells expressing either Rab5 or Rab11 biosensors into portions of 10–12 adjacent pixels, thus generating multiple abundance and activity data for each single snapshot. For each region, we measured mean fluorescence intensities and FRET efficiency values and then we computed the Loop IDX (Materials and Methods). By juxtaposing these estimates over time, we reconstructed the spatiotemporal dynamics of abundance, biochemical activity, and Loop IDX for both Rab5 and Rab11 at the endocytic surface (Figures S9A and S9B).

In our time-series data, we noticed that Rab5 and Rab11 at the endocytic surface might cluster, appearing as patches, with either blurred or sharp outlines and displaying transient changes in GTPase biochemical activation for both control and Zfyve26 condition (Figures S9A and S9B, left and middle panels). Similarly, we found that both Rab5 and Rab11 Loop IDXs varied during time, thus resulting in membrane regions marked by either negative (blue), null (white) or positive (orange) Loop IDX values (Figures S9A and S9B, right panels). In particular, we found positive, null, and negative Rab5 Loop IDX values at the surface of endocytic structures in control cells (Figure S9A, top right panel, blue, white, orange areas). On the contrary, an overall increase in Rab5 Loop IDX was observed upon Zfyve26 expression, as displayed by the elevated frequency of orange regions at the surface (Figure S9A, bottom right panels, orange). Instead, differences in Rab11 Loop IDX between control and Zfyve26 expressing cells showed a more regional labeling (Figure S9B, top and bottom right panels).

Next, we focused our attention on local patterns that might arise at the surface of both control and Zfyve26 endosomes (Figures 6A and 6B). Specifically, we compared both FRET efficiency and Loop IDX in regions characterized by either low or high Rab levels. We found that changes in Rab5 levels were not associated to relevant differences in both FRET efficiency and Loop IDX in the control (Figure 6A, control condition, α, β panels). In marked contrast, higher FRET efficiency and positive Loop IDX characterized membrane portions with elevated Rab5 in Zfyve26 condition (Figure 6A, Zfyve26 condition, γ, δ panels). Unexpectedly, such regions with higher FRET efficiency were associated to reduced Loop IDX values (Figure 6A, Zfyve26 condition, δ panel). Correlation analysis confirmed the negative association between Loop IDX and FRET efficiency for Rab5 (Figures 6C and 6E, green line). Similar results were obtained for Rab11 labeled regions (Figure 6B, α-δ panels; Figure 6E, pink line). Of note, opposite observations were made for this control endosome where we found the uncoupling between Loop IDX and the corresponding GTPase activation status (Figures 6C and 6E, light green line; Figure 6E, light pink line). Therefore, these data suggest that, when linked to variation in Rab activation status, Loop IDX changes might reflect the presence of saturating Zfyve26 amounts.

To assess whether correlation changes between Loop IDX and FRET efficiency can inform about biochemical saturation reached by the Rab effector in GTPase network, we performed stochastic simulations using incremental amounts of Rab effector until the equimolarity between the total GTPase pool and the Rab effector was reached. Note that among the 32 theoretical models we developed, we used the competitive model III for this analysis, as it was found to generate changes in correlation values (i.e., increase/decrease) in response to effector level, similar to our experimental data (Figures 2 and S7, Table 1).

The shared effector was allowed to change stochastically around a fixed mean value ($\langle E \rangle$ = 0, 100, 200, 400, Materials and methods), thus generating fluctuations. We found changes and dampening in the trajectory's amplitude for both Rab^{GTP} and Rab_{Mem} when the $\langle E \rangle$ level reached equimolarity with the total GTPase pool (i.e., 400 molecules) (Figure S10A,

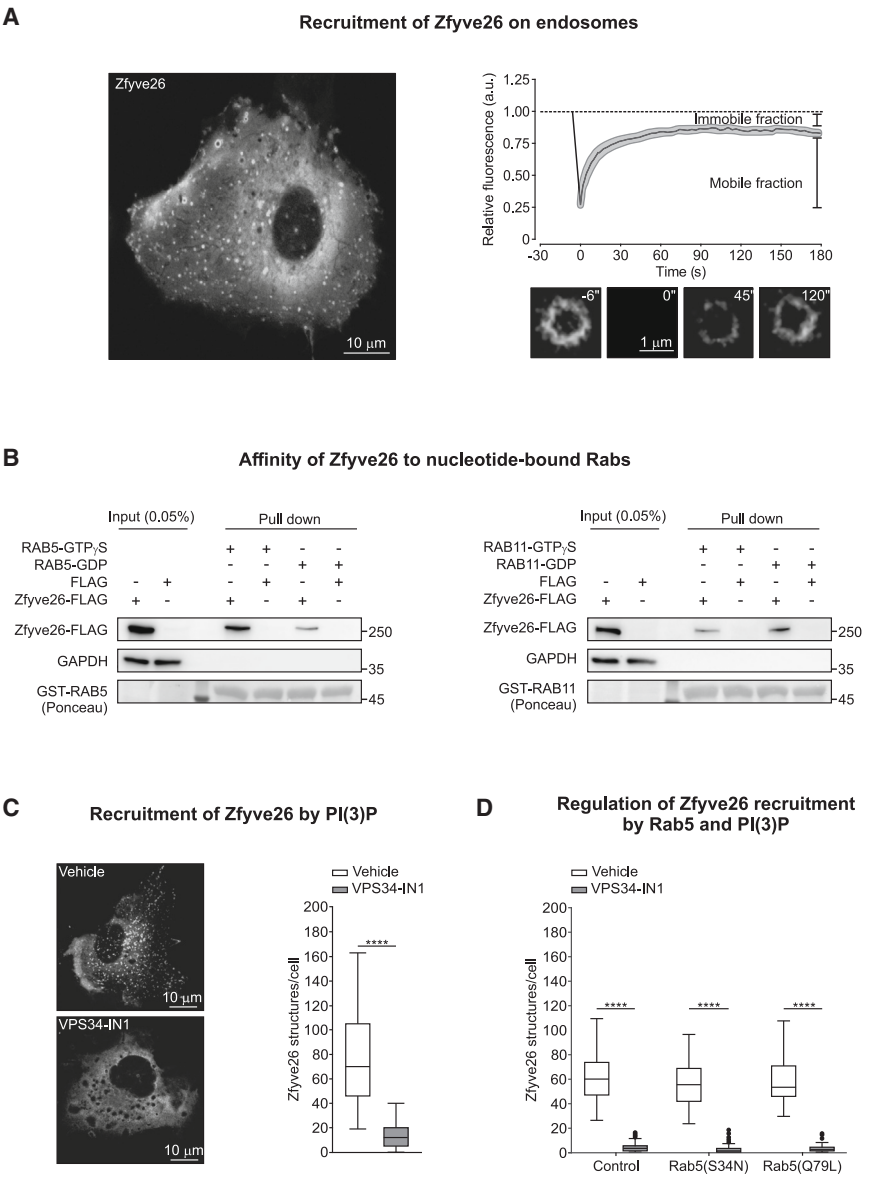

Figure 5. Zfyve26 localization on endosomes relies on phosphatidylinositol 3-phosphate

(A) Quantification of fluorescence recovery after photo bleaching (FRAP) on GFP-Zfyve26-positive spherical endosomes. Representative image of a cell expressing GFP-Zfyve26 (left). Quantification and representative time course images of a photobleaching experiments (right panels). Gray area represents standard error of mean (SEM) of data. n = 20 GFP-Zfyve26-positive spherical endosomes.

(B) Representative western blot of Zfyve26 binding to recombinant GDP- or GTPγS-bound Rab5 by pull-down assay (left panel), n = 3 independent experiments. Representative western blot of Zfyve26 binding to recombinant GDP- or GTPγS-bound Rab11 by pull-down assay (right panel), n = 3 independent experiments.

(C) Quantification of the number of GFP-Zfyve26 positive structures per single cell upon treatment with VPS34-IN1, a PIK3C3 inhibitor. Representative images of GFP-Zfyve26 positive structures in control (vehicle, top left panel) or treated (VPS34-IN1, bottom left panel) conditions and quantification (right panel). Boxplots indicate median (middle line), 25th, 75th percentile (box) and 5th and 95th percentile (whiskers). **** p value <0.0001 (Kolmogorov-Smirnov test), n = 61 cells in control condition, n = 67 cells in treated cells.

(D) Quantification of the number of GFP-Zfyve26 structures in cells co-expressing GFP-Zfyve26/mCherry (control), GFP-Zfyve26/mCherry-Rab5(S34N) (Rab5(S34N)), GFP-Zfyve26/mCherry-Rab5(Q79L) (Rab5(Q79L)),treated with either DMSO (vehicle) or VPS34-IN1 inhibitor (VPS34-IN1). Boxplots indicate median (middle line), 25th, 75th percentile (box) and 5th and 95th percentile (whiskers) as well as outliers (single points). **** p value <0.0001 (Kolmogorov-Smirnov test), n = 50 cells in control condition (vehicle), n = 48 cells in Rab5(S34N) condition (vehicle), n = 48 cells in Rab5(Q79L) condition (vehicle), n = 50 cells in control condition (VPS34-IN1), n = 55 cells in Rab5(S34N) condition (VPS34-IN1), n = 50 cells in Rab5(Q79L) condition (VPS34-IN1).

Materials and methods). Next, we sampled our simulations for each fixed $\langle E \rangle$ condition and we computed: (1) the mean Rab^{GTP} ($\langle Rab^{GTP} \rangle$), (2) the mean Rab_{Mem} (i.e., $\langle Rab_{Mem} \rangle$) and (3) the Loop IDX (i.e., $\rho(Rab_{Mem}, Rab^{GTP})$). Such approach revealed distributions of subsampled values for both active GTPase and Loop IDX at different Zfyve26 levels (Figure S10B and S10C). Using these distributions, we performed correlation analysis to determine whether Rab^{GTP} and Loop IDX are correlated when Zfyve26 reaches saturation.

Our simulations indicated that the mean GTPase activation status and the Loop IDX negatively correlated when the Zfyve26 level approached saturation (Figures 6D and 6F). In particular, we found uncorrelated Loop IDX and GTPase activation status values at non-saturating Zfyve26 mean amounts (n = 0, 50, 200 molecules, Figures 6D and 6F), whereas negative correlation was found at saturating Zfyve26 level for both GTPases, thus supporting our experimental results (n = 400 molecules, Figures 6D and 6F, green and pink lines). This finding can be explained by the fact that in our closed system a saturating effector amount leads the entire GTPase pool to be retained on the membrane. Thus, by reaching such maximum threshold level, fluctuations between the membrane and the GTP-bound fraction of GTPase molecules are dampened. Consequently, the correlation between the Loop IDX and the mean GTP-bound fraction of Rabs decreased.

These data suggest that the correlation between the Loop IDX and the amount of active GTPase might inform about the Zfyve26 saturation level, null for unsaturated and negative for Zfyve26 saturated system, a finding that does not rely on the type of self-regulatory loop controlling Rab11 functioning, as demonstrated by performing a similar computation using model IV (Figures S10D and S10E). Overall, by using fluctuations of the Loop IDX, we demonstrated the potential of correlation analysis

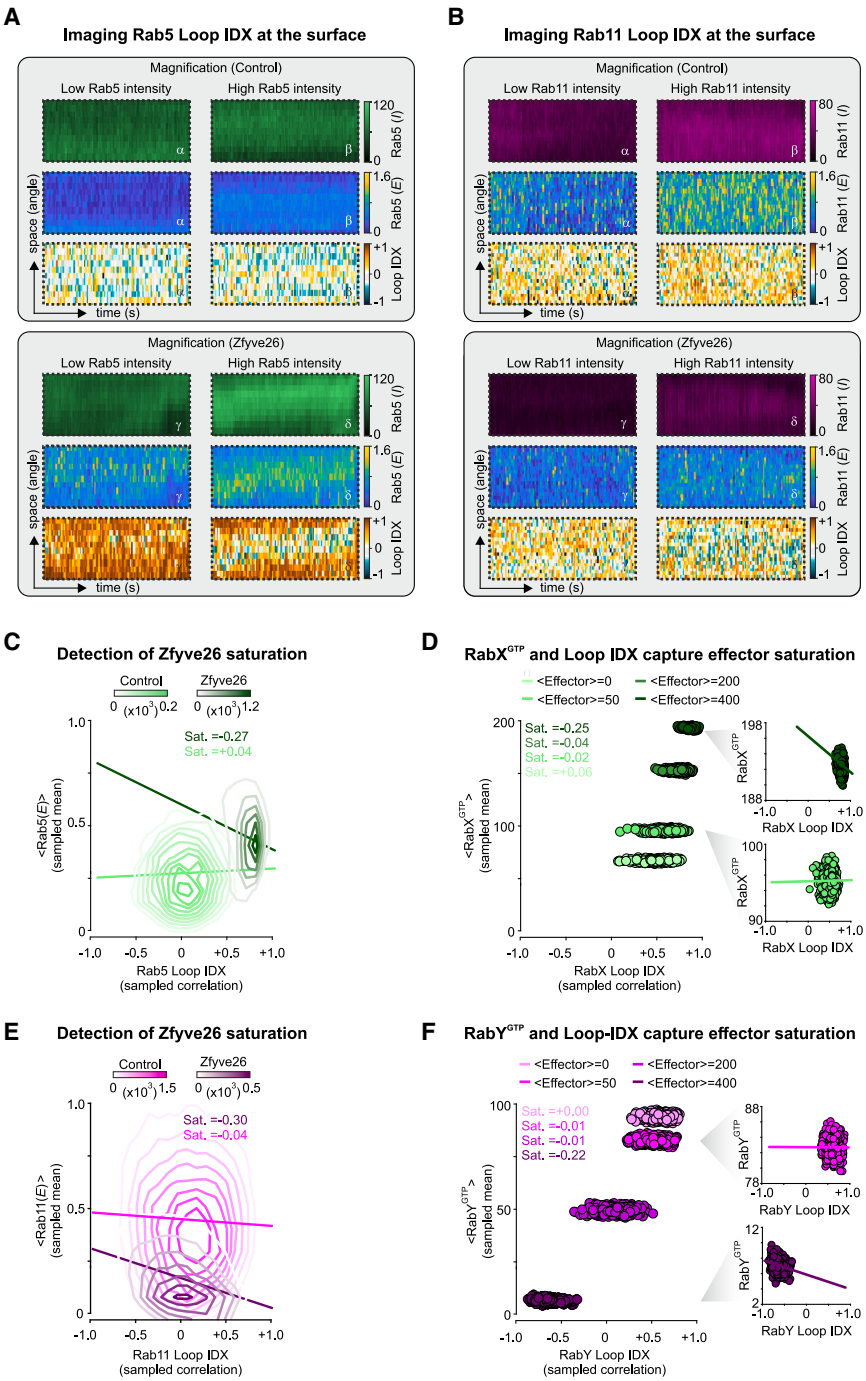

Figure 6. Correlations analysis captures Zfyve26 saturation at the endocytic surface by using loop index

(A) Representative magnification of the Rab5 Loop IDX at the surface of a single endocytic organelle resulting from kymograph data in both control (top panels) and Zfyve26 expressing cells (bottom panels). Black-to-green, blue-to-yellow and blue-to-orange gradients represent Rab5 abundance, Rab5 FRET efficiency and Rab5 Loop IDX, respectively.

(B) Representative magnification of the Rab11 Loop IDX at the surface of a single endocytic organelle resulting from kymograph data in both control (top panels) and Zfyve26 expressing cells (bottom panels). Black-to-magenta, blue-to-yellow and blue-to-orange gradients represent Rab11 abundance, Rab11 FRET efficiency and Rab11 Loop IDX, respectively.

(C) Scatterplot of both Rab5 activity (i.e., Rab5 (*E*)) and Rab5 Loop IDX measured for both control and Zfyve26 expressing cells transfected with Rab5 activity sensor. White-to-green gradient represents data density for control cells. White-to-dark green gradient represents data density for Zfyve26 expressing cells. Lines represent the correlation (Saturation, Sat.) values (n = 10800 subsampled values).

(D) Scatterplot of subsampled RabX activity and RabX Loop IDX at different effector level (0, 50, 200, and 400) using model III. Data magnification for high (top left, 400) and low (bottom left, 50) effector values are displayed. Dots of different green shades represent values obtained at different effector level. (n simulations = 5 × 10,[4] subsampled in batches of n = 50).

(E) Scatterplot of both Rab11 activity (i.e., Rab11 (*E*)) and Rab11 Loop IDX measured for both control and Zfyve26 expressing cells transfected with Rab11 activity sensor. White-to-magenta gradient represents data density for control cells. White-to-dark magenta gradient represents data density for Zfyve26 expressing cells. Lines represent the correlation (Saturation, Sat.) values (n = 10800 subsampled values).

(F) Scatterplot of subsampled RabY activity and RabY Loop IDX at different effector level (0, 50, 200, and 400) using model III. Data magnification for high (top left, 400) and low (bottom left, 50) effector values are displayed. Dots of different magenta shades represent values obtained at different effector level. (n simulations = 5 × 10,[4] subsampled in batches of n = 50).

in detecting Zfyve26 saturation at the surface of a single endosome, a condition that was mimicked by our stochastic competitive model of Rab5 and Rab11 network.

DISCUSSION

Specificity in membrane trafficking relies on the interaction between Rab small GTPase proteins and their molecular effectors.[3] However, the evidence that many Rab proteins can bind to a single effector challenges this view. Using correlation analysis applied to FRET imaging, we identified molecular competition as a novel design that ensures Rab cross-regulation at the surface of a single endocytic organelle.

In principle, a Rab competition network works in an indirect fashion compared to a Rab cascade,[3,8,9,33] forming a hidden layer of regulation, that copes with the elevated number of biological

functions carried out by such transducers in membrane trafficking (e.g., fusion, fission, tethering). Our simulations show that the competition for a common effector is central to the production of a more versatile crosstalk scheme in Rab signaling, which depends on component's concentration and binding affinities for each possible interaction. Through the combinatorial formation of protein complexes, both abundance and activation status of Rab proteins are linked in terms of fluctuations. Accordingly, our correlation analysis showed co-occurrent variations in potential yet hypothetical Rab circuits in response to variation in effector levels. These findings were further confirmed by our live-cell imaging experiments using Rab5 and Rab11 as a case of study. These results demonstrate that correlated changes in the abundance and/or activation status of GTPase signaling are a key feature of the Rab competition hypothesis.

Of particular concern in the Rab competition hypothesis are the binding modalities of the players involved in the interaction network. The key factor for Rab competition is the mutual association with intermediary molecular species, regardless of whether such interaction is direct or mediated through intervening proteins (i.e., indirect). Consequently, interactions with unclear binding modalities, such as those obtained using affinity purification columns—a standard approach in Rab effector identification—can still suggest for proteins that could, potentially, generate Rab competition. In this context, our imaging and biochemical data on Zfyve26 support this view. Nonetheless, our study lacks a detailed analysis of the Zfyve26 protein surface that binds either directly or indirectly to Rab5/Rab11. The finding that the Zfyve26^{L243P} variant, which is known to cause Spastic Paraplegia 15, abrogates Rab5/Rab11 interactions, corroborate our findings and suggest potential Zfyve26's regions involved in GTPase interaction.[23]

Our work provides a conceptual advance in the modeling and analysis of Rab circuits. Motivated by the *in vitro* evidence of stochasticity of Rab reaction network components,[6,7] we developed the Loop index (Loop IDX) to link the GTPase biochemical activation status to its abundance at the membrane, thus providing a snapshot of molecular fluctuations in Rab activation circuits. Using the Loop IDX, we found that Zfyve26, a Rab5 and Rab11 binding protein recruited to membranes by the PI(3)P lipid, acts as a surface cue on endosomes, by controlling the relationship between GTPase activation status variations and its abundance. This challenges the notion that Rab's membrane accumulation is a proxy of GTPase activation, as indicated by our time lapse experiments using the Rab5 FRET probe, whereas still confirms the fundamental role of regulatory loops such as feedbacks in GTPase patterning.[6,7,25]

An important aspect of the Loop IDX is that it allows, by comparing control and perturbed cells, to discern between distinct regulatory motifs controlling small GTPase switching. In particular, using the Loop IDX we provide indications that a feedforward loop, in which the activation of Rab11 GEFs is triggered by inactive Rab11, might control Rab11 cycling at the surface of a Rab5-positive organelle. Such a rapid conversion of Rab11 molecules from their inactive to their active form is consistent with the need to limit endosome tubulation caused by an excess of inactive Rab11.[28] In addition, the fact that the Rab11 feedforward loop does not induce the active GTPase to recruit GEF proteins is in line with the absence of an enlarged Rab11 membrane domain on the Rab5-positive organelle.[7,9] This suggests that proteins controlling Rab11 feedback may be located in the recycling endosomal compartment, rather than in the Rab5-positive endosome, where Rab11 accumulates and where higher Loop IDXs are likely to occur.

Another aspect of the Loop IDX is that it is formulated without any preconceptions about the position of the Rab GTPases, their mutual localization, or the chronological order of the time-lapse series data. This approach reflects the lack of prior knowledge about the biological processes taking place at the time of analysis, a condition that occurs when studying signaling mechanisms at the surface of submicrometric cellular structures. However, Loop IDX alone, as a correlational measure, does not assess cause-effect relationships and additional information is required to effectively discriminate among different regulatory motifs by using this metric.[34–36] With these considerations in mind, we explored the employment of Loop IDX to infer Zfyve26 saturation in the Rab5-Rab11 competition network. Simulations and experiments confirm the validity of this approach thus indicating that the Loop IDX will be a significant step forward in the characterization of Rab GTPase systems *in vivo*.

The ability to parse out cellular signaling events in time and space would help to identify functional motifs in biochemical reaction networks. The cooperative action of Rab reaction network components was proven sufficient to generate switch-like, ultrasensitive responses ensuring specificity in membrane trafficking.[25,37,38] Notably, activation of this Rab network can occur stochastically when fluctuations in protein levels reach a critical threshold resulting in spatial patterning and traveling waves of activated biomolecular switches.[6,7] Our findings extended these concepts, by providing the evidence that signal transduction in the endocytic system can be controlled by stochiometric constraints of competing functionally interacting components. This has profound implications when studying the role of proteins involved in autosomal recessive genetic disease such as Spastic Paraplegia 15, in which detrimental mutations in Zfyve26 alter binding affinities and hence stoichiometry of multiprotein complexes involved in maturation of endosomes along the endocytic pathway.[22,23,39–43] Therefore, in the control of trafficking specificity, a more versatile crosstalk scheme may arise from fluctuations of shared effector, that connect different Rab signaling pathways even without their direct physical interaction.

Limitations of the study

Owing to the intricate structural complexity of Zfyve26, we were unable to precisely delineate the specific region of the protein responsible for interacting with both Rab5 and Rab11, which mediates the competitive interactions observed in this study. To date, no evidence has been published confirming a direct physical interaction between Zfyve26 and Rab5/Rab11.

RESOURCE AVAILABILITY

Lead contact

Further information and requests for scripts, resources, and reagents should be directed to and will be fulfilled by lead contact, Carlo Cosimo Campa (carlocosimo.campa@iigm.it).

Materials availability

All materials supporting the findings of this study are available from the corresponding authors upon reasonable request.

Data and code availability

- Data: All data reported in this paper will be shared by the lead contact upon request.
- Code: All original code has been deposited at Code Ocean and is publicly available at Code Ocean: https://doi.org/10.24433/CO.5317183.v1; Code Ocean: https://doi.org/10.24433/CO.9194314.v1; Code Ocean: https://doi.org/10.24433/CO.3851388.v1 as of the date of publication.
- Additional information: Any additional information required to reanalyze the data reported in this paper is available from the lead contact upon request.

ACKNOWLEDGMENTS

We are grateful to Mukhran Khundadze, Christian Hübner (Institute of Human Genetics, University Hospital, Jena, Germany) and Michiyuki Matsuda (Department of Pathology and Biology of Diseases, Graduate School of Medicine, Kyoto University, Japan) for sharing reagents. This work was supported by an internal grant program of the Italian Institute for Genomic Medicine (to C.C.C.) The research leading to these results has received funding from AIRC under MFAG 2020-ID. 24897 project–P.I. CC and from Telethon-CARIPLO research grant (GJC22068 to C.C.C.). E.H. was supported by Associazione Italiana Ricerca Cancro (AIRC 21875), J.P.M. was supported by postdoctoral fellowships of the Fondazione Umberto Veronesi (FUV) and Associazione Italiana Ricerca sul Cancro fellowships (AIRC 22558). M.C.D.S was supported by postdoctoral fellowships of the Associazione Italiana Ricerca sul Cancro (AIRC 28201).

AUTHOR CONTRIBUTIONS

E.F. performed mathematical simulations, analyzed the data, and wrote the manuscript; S.T., J.P.M, L.G., and M.C.D.S. performed experiments and analyzed the data, M.C. analyzed the data, C.E.B. provided a segmentation code draft, I.F. and E.H. provided reagents and comments, C.E.B., A.G., and A.P. provided suggestions; C.B. and C.C.C. conceived and designed the experiments and wrote the manuscript. All authors reviewed the paper and provided comments.

DECLARATION OF INTERESTS

EH is a founder of Kither Biotech, a company involved in the development of PI3K inhibitors. E.H. and C.C.C. own patents related to quantification of Rab11 activity.

DECLARATION OF GENERATIVE AI AND AI ASSISTED TECHNOLOGIES

During the preparation of this work the authors used Microsoft Copilot in order to improve the clarity of the text. After using this service, the authors reviewed and edited the content as needed and take full responsibility for the content of the publication.

STAR★METHODS

Detailed methods are provided in the online version of this paper and include the following:

SUPPLEMENTAL INFORMATION

Supplemental information can be found online at https://doi.org/10.1016/j.isci.2025.112170.

Received: November 25, 2024
Revised: January 18, 2025
Accepted: March 3, 2025
Published: March 6, 2025

REFERENCES

1. Zerial, M., and McBride, H. (2001). Rab proteins as membrane organizers. Nat. Rev. Mol. Cell Biol. *2*, 107–117. https://doi.org/10.1038/35052055.
2. Sönnichsen, B., De Renzis, S., Nielsen, E., Rietdorf, J., and Zerial, M. (2000). Distinct membrane domains on endosomes in the recycling pathway visualized by multicolor imaging of Rab4, Rab5, and Rab11. J. Cell Biol. *149*, 901–914. https://doi.org/10.1083/jcb.149.4.901.
3. Grosshans, B.L., Ortiz, D., and Novick, P. (2006). Rabs and their effectors: achieving specificity in membrane traffic. Proc. Natl. Acad. Sci. USA *103*, 11821–11827. https://doi.org/10.1073/pnas.0601617103.
4. Campa, C.C., and Hirsch, E. (2017). Rab11 and phosphoinositides: A synergy of signal transducers in the control of vesicular trafficking. Adv. Biol. Regul. *63*, 132–139. https://doi.org/10.1016/j.jbior.2016.09.002.
5. Kholodenko, B.N. (2006). Cell-signalling dynamics in time and space. Nat. Rev. Mol. Cell Biol. *7*, 165–176. https://doi.org/10.1038/nrm1838.
6. Bezeljak, U., Loya, H., Kaczmarek, B., Saunders, T.E., and Loose, M. (2020). Stochastic activation and bistability in a Rab GTPase regulatory network. Proc. Natl. Acad. Sci. USA *117*, 6540–6549. https://doi.org/10.1073/pnas.1921027117.

7. Cezanne, A., Lauer, J., Solomatina, A., Sbalzarini, I.F., and Zerial, M. (2020). A non-linear system patterns Rab5 GTPase on the membrane. Elife *9*, e54434. https://doi.org/10.7554/eLife.54434.

8. Tsyganov, M.A., Kolch, W., and Kholodenko, B.N. (2012). The topology design principles that determine the spatiotemporal dynamics of G-protein cascades. Mol. Biosyst. *8*, 730–743. https://doi.org/10.1039/c2mb05375f.

9. Del Conte-Zerial, P., Brusch, L., Rink, J.C., Collinet, C., Kalaidzidis, Y., Zerial, M., and Deutsch, A. (2008). Membrane identity and GTPase cascades regulated by toggle and cut-out switches. Mol. Syst. Biol. *4*, 206. https://doi.org/10.1038/msb.2008.45.

10. Shirane, M., and Nakayama, K.I. (2006). Protrudin induces neurite formation by directional membrane trafficking. Science *314*, 818–821. https://doi.org/10.1126/science.1134027.

11. Gillingham, A.K., Sinka, R., Torres, I.L., Lilley, K.S., and Munro, S. (2014). Toward a comprehensive map of the effectors of rab GTPases. Dev. Cell *31*, 358–373. https://doi.org/10.1016/j.devcel.2014.10.007.

12. Gillingham, A.K., Bertram, J., Begum, F., and Munro, S. (2019). In vivo identification of GTPase interactors by mitochondrial relocalization and proximity biotinylation. Elife *8*, e45916. https://doi.org/10.7554/eLife.45916.

13. Solinger, J.A., Rashid, H.O., and Spang, A. (2022). FERARI and cargo adaptors coordinate cargo flow through sorting endosomes. Nat. Commun. *13*, 4620. https://doi.org/10.1038/s41467-022-32377-y.

14. Solinger, J.A., Rashid, H.O., Prescianotto-Baschong, C., and Spang, A. (2020). FERARI is required for Rab11-dependent endocytic recycling. Nat. Cell Biol. *22*, 213–224. https://doi.org/10.1038/s41556-019-0456-5.

15. de Renzis, S., Sönnichsen, B., and Zerial, M. (2002). Divalent Rab effectors regulate the sub-compartmental organization and sorting of early endosomes. Nat. Cell Biol. *4*, 124–133. https://doi.org/10.1038/ncb744.

16. Rai, A., Goody, R.S., and Müller, M.P. (2019). Multivalency in Rab effector interactions. Small GTPases *10*, 40–46. https://doi.org/10.1080/21541248.2016.1265700.

17. Klumpe, H.E., Garcia-Ojalvo, J., Elowitz, M.B., and Antebi, Y.E. (2023). The computational capabilities of many-to-many protein interaction networks. Cell Syst. *14*, 430–446. https://doi.org/10.1016/j.cels.2023.05.001.

18. Bosia, C., Sgrò, F., Conti, L., Baldassi, C., Brusa, D., Cavallo, F., Cunto, F.D., Turco, E., Pagnani, A., and Zecchina, R. (2017). RNAs competing for microRNAs mutually influence their fluctuations in a highly non-linear microRNA-dependent manner in single cells. Genome Biol. *18*, 37. https://doi.org/10.1186/s13059-017-1162-x.

19. Del Giudice, M., Bosia, C., Grigolon, S., and Bo, S. (2018). Stochastic sequestration dynamics: a minimal model with extrinsic noise for bimodal distributions and competitors correlation. Sci. Rep. *8*, 10387. https://doi.org/10.1038/s41598-018-28647-9.

20. Brodland, G.W. (2015). How computational models can help unlock biological systems. Semin. Cell Dev. Biol. *47–48*, 62–73. https://doi.org/10.1016/j.semcdb.2015.07.001.

21. Redpath, G.M.I., Ecker, M., Kapoor-Kaushik, N., Vartoukian, H., Carnell, M., Kempe, D., Biro, M., Ariotti, N., and Rossy, J. (2019). Flotillins promote T cell receptor sorting through a fast Rab5-Rab11 endocytic recycling axis. Nat. Commun. *10*, 4392. https://doi.org/10.1038/s41467-019-12352-w.

22. Hirst, J., Borner, G.H.H., Edgar, J., Hein, M.Y., Mann, M., Buchholz, F., Antrobus, R., and Robinson, M.S. (2013). Interaction between AP-5 and the hereditary spastic paraplegia proteins SPG11 and SPG15. Mol. Biol. Cell *24*, 2558–2569. https://doi.org/10.1091/mbc.E13-03-0170.

23. Vantaggiato, C., Panzeri, E., Castelli, M., Citterio, A., Arnoldi, A., Santorelli, F.M., Liguori, R., Scarlato, M., Musumeci, O., Toscano, A., et al. (2019). ZFYVE26/SPASTIZIN and SPG11/SPATACSIN mutations in hereditary spastic paraplegia types AR-SPG15 and AR-SPG11 have different effects on autophagy and endocytosis. Autophagy *15*, 34–57. https://doi.org/10.1080/15548627.2018.1507438.

24. Prekeris, R., Klumperman, J., and Scheller, R.H. (2000). A Rab11/Rip11 protein complex regulates apical membrane trafficking via recycling endosomes. Mol. Cell *6*, 1437–1448. https://doi.org/10.1016/s1097-2765(00)00140-4.

25. Lippe, R., Miaczynska, M., Rybin, V., Runge, A., and Zerial, M. (2001). Functional synergy between Rab5 effector Rabaptin-5 and exchange factor Rabex-5 when physically associated in a complex. Mol. Biol. Cell *12*, 2219–2228. https://doi.org/10.1091/mbc.12.7.2219.

26. Rink, J., Ghigo, E., Kalaidzidis, Y., and Zerial, M. (2005). Rab conversion as a mechanism of progression from early to late endosomes. Cell *122*, 735–749. https://doi.org/10.1016/j.cell.2005.06.043.

27. Kitano, M., Nakaya, M., Nakamura, T., Nagata, S., and Matsuda, M. (2008). Imaging of Rab5 activity identifies essential regulators for phagosome maturation. Nature *453*, 241–245. https://doi.org/10.1038/nature06857.

28. Campa, C.C., Margaria, J.P., Derle, A., Del Giudice, M., De Santis, M.C., Gozzelino, L., Copperi, F., Bosia, C., and Hirsch, E. (2018). Rab11 activity and PtdIns(3)P turnover removes recycling cargo from endosomes. Nat. Chem. Biol. *14*, 801–810. https://doi.org/10.1038/s41589-018-0086-4.

29. Stenmark, H., Parton, R.G., Steele-Mortimer, O., Lütcke, A., Gruenberg, J., and Zerial, M. (1994). Inhibition of rab5 GTPase activity stimulates membrane fusion in endocytosis. EMBO J. *13*, 1287–1296. https://doi.org/10.1002/j.1460-2075.1994.tb06381.x.

30. Khundadze, M., Kollmann, K., Koch, N., Biskup, C., Nietzsche, S., Zimmer, G., Hennings, J.C., Huebner, A.K., Symmank, J., Jahic, A., et al. (2013). A hereditary spastic paraplegia mouse model supports a role of ZFYVE26/SPASTIZIN for the endolysosomal system. PLoS Genet. *9*, e1003988. https://doi.org/10.1371/journal.pgen.1003988.

31. Sorribas, A., Hernández-Bermejo, B., Vilaprinyo, E., and Alves, R. (2007). Cooperativity and saturation in biochemical networks: a saturable formalism using Taylor series approximations. Biotechnol. Bioeng. *97*, 1259–1277. https://doi.org/10.1002/bit.21316.

32. Chen, B.-S., Wu, W.-S., Wang, Y.-C., and Li, W.-H. (2007). On the robust circuit design schemes of biochemical networks: steady-state approach. IEEE Trans. Biomed. Circuits Syst. *1*, 91–104. https://doi.org/10.1109/TBCAS.2007.907060.

33. Rivera-Molina, F.E., and Novick, P.J. (2009). A Rab GAP cascade defines the boundary between two Rab GTPases on the secretory pathway. Proc. Natl. Acad. Sci. USA *106*, 14408–14413. https://doi.org/10.1073/pnas.0906536106.

34. Noh, J., Isogai, T., Chi, J., Bhatt, K., and Danuser, G. (2022). Granger-causal inference of the lamellipodial actin regulator hierarchy by live cell imaging without perturbation. Cell Syst. *13*, 471–487.e8. https://doi.org/10.1016/j.cels.2022.05.003.

35. Zaritsky, A., Tseng, Y.Y., Rabadán, M.A., Krishna, S., Overholtzer, M., Danuser, G., and Hall, A. (2017). Diverse roles of guanine nucleotide exchange factors in regulating collective cell migration. J. Cell Biol. *216*, 1543–1556. https://doi.org/10.1083/jcb.201609095.

36. Lee, K., Elliott, H.L., Oak, Y., Zee, C.T., Groisman, A., Tytell, J.D., and Danuser, G. (2015). Functional hierarchy of redundant actin assembly factors revealed by fine-grained registration of intrinsic image fluctuations. Cell Syst. *1*, 37–50. https://doi.org/10.1016/j.cels.2015.07.001.

37. Delprato, A., and Lambright, D.G. (2007). Structural basis for Rab GTPase activation by VPS9 domain exchange factors. Nat. Struct. Mol. Biol. *14*, 406–412. https://doi.org/10.1038/nsmb1232.

38. Zhang, Z., Zhang, T., Wang, S., Gong, Z., Tang, C., Chen, J., and Ding, J. (2014). Molecular mechanism for Rabex-5 GEF activation by Rabaptin-5. Elife *3*, e02687. https://doi.org/10.7554/eLife.02687.

39. Vantaggiato, C., Orso, G., Guarato, G., Brivio, F., Napoli, B., Panzeri, E., Masotti, S., Santorelli, F.M., Lamprou, M., Gumeni, S., et al. (2023). Rescue of lysosomal function as therapeutic strategy for SPG15 hereditary spastic paraplegia. Brain *146*, 1103–1120. https://doi.org/10.1093/brain/awac308.

40. Chang, J., Lee, S., and Blackstone, C. (2014). Spastic paraplegia proteins spastizin and spatacsin mediate autophagic lysosome reformation. J. Clin. Investig. *124*, 5249–5262. https://doi.org/10.1172/JCI77598.

41. Saffari, A., Kellner, M., Jordan, C., Rosengarten, H., Mo, A., Zhang, B., Strelko, O., Neuser, S., Davis, M.Y., Yoshikura, N., et al. (2023). The clinical and molecular spectrum of ZFYVE26-associated hereditary spastic paraplegia: SPG15. Brain *146*, 2003–2015. https://doi.org/10.1093/brain/awac391.

42. Hirst, J., Hesketh, G.G., Gingras, A.C., and Robinson, M.S. (2021). Rag GTPases and phosphatidylinositol 3-phosphate mediate recruitment of the AP-5/SPG11/SPG15 complex. J. Cell Biol. *220*, e202002075. https://doi.org/10.1083/jcb.202002075.

43. Khundadze, M., Ribaudo, F., Hussain, A., Stahlberg, H., Brocke-Ahmadinejad, N., Franzka, P., Varga, R.E., Zarkovic, M., Pungsrinont, T., Kokal, M., et al. (2021). Mouse models for hereditary spastic paraplegia uncover a role of PI4K2A in autophagic lysosome reformation. Autophagy *17*, 3690–3706. https://doi.org/10.1080/15548627.2021.1891848.

44. Blumer, J., Rey, J., Dehmelt, L., Mazel, T., Wu, Y.W., Bastiaens, P., Goody, R.S., and Itzen, A. (2013). RabGEFs are a major determinant for specific Rab membrane targeting. J. Cell Biol. *200*, 287–300. https://doi.org/10.1083/jcb.201209113.

45. Esters, H., Alexandrov, K., Iakovenko, A., Ivanova, T., Thomä, N., Rybin, V., Zerial, M., Scheidig, A.J., and Goody, R.S. (2001). Vps9, Rabex-5 and DSS4: proteins with weak but distinct nucleotide-exchange activities for Rab proteins. J. Mol. Biol. *310*, 141–156. https://doi.org/10.1006/jmbi.2001.4735.

46. Rybin, V., Ullrich, O., Rubino, M., Alexandrov, K., Simon, I., Seabra, M.C., Goody, R., and Zerial, M. (1996). GTPase activity of Rab5 acts as a timer for endocytic membrane fusion. Nature *383*, 266–269. https://doi.org/10.1038/383266a0.

47. Gavriljuk, K., Gazdag, E.M., Itzen, A., Kötting, C., Goody, R.S., and Gerwert, K. (2012). Catalytic mechanism of a mammalian Rab.RabGAP complex in atomic detail. Proc. Natl. Acad. Sci. USA *109*, 21348–21353. https://doi.org/10.1073/pnas.1214431110.

48. Kardash, E., Bandemer, J., and Raz, E. (2011). Imaging protein activity in live embryos using fluorescence resonance energy transfer biosensors. Nat. Protoc. *6*, 1835–1846. https://doi.org/10.1038/nprot.2011.395.

49. Pelkmans, L., Kartenbeck, J., and Helenius, A. (2001). Caveolar endocytosis of simian virus 40 reveals a new two-step vesicular-transport pathway to the ER. Nat. Cell Biol. *3*, 473–483. https://doi.org/10.1038/35074539.

50. Carpenter, A.E., Jones, T.R., Lamprecht, M.R., Clarke, C., Kang, I.H., Friman, O., Guertin, D.A., Chang, J.H., Lindquist, R.A., Moffat, J., et al. (2006). CellProfiler: image analysis software for identifying and quantifying cell phenotypes. Genome Biol. *7*, R100. https://doi.org/10.1186/gb-2006-7-10-r100.

51. Gillespie, D.T. (1976). A general method for numerically simulating the stochastic time evolution of coupled chemical reactions. J. Comput. Phys. *22*, 403–434. https://doi.org/10.1016/0021-9991(76)90041-3.

52. Dw Frost, S. (2016). Gillespie.jl: Stochastic Simulation Algorithm in Julia. J. Open Source Softw. *1*, 42. https://doi.org/10.21105/joss.00042.

STAR★METHODS

KEY RESOURCES TABLE

REAGENT or RESOURCE	SOURCE	IDENTIFIER
Antibodies		
Rab11 (D4F5)	Cell Signaling Technology	Cat# 5589; RRID: AB_10692655
Rab5	BD Biosciences	Cat# 610725; RRID: AB_398142
PI(3)P	Echelon Biosciences	Cat# Z-P003; RRID: AB_2891181
Rab11	BD Biosciences	Cat# 610656; RRID: AB_397990
Rab5A (E6N8S)	Cell Signaling Technology	Cat# 46449; RRID: AB_2799100
GFP (4B10)	Cell Signaling Technology	Cat# 2955; RRID: AB_1196615
GAPDH	Proteintech	Cat# 60004-1; RRID: AB_2107436
Anti-mouse/rabbit IgG Atto 488	Sigma-Aldrich	Cat# 18772; RRID: AB_2535792
Anti-mouse IgG Atto 550	Sigma-Aldrich	Cat# 43394; RRID: AB_2532079
Anti-rabbit IgG 647 Alexa-Fluor	Invitrogen	Cat# A32733TR; RRID: AB_2633282
Anti-Mouse IgG HRP	Sigma-Aldrich	Cat# A4416; RRID: AB_258284
Anti-Rabbit IgG HRP	Sigma-Aldrich	Cat# A6154; RRID: AB_258284
Bacterial and virus strains		
BL21 (DE3)	Thermofisher	Cat# EC0114
p ZFYVE26	Christian Hübner lab	
p Raichu-Rab5	Michiyuki Matsuda lab	
p AS-Rab11	Emilio Hirsch lab	
p mEGFP-Rab11	Emilio Hirsch lab	
p mEGFP-Rab5	Emilio Hirsch lab	
p mCherry-Rab11a	Addgene	Cat# 55124; RRID: Addgene_55124
p mCherry-Rab5	This paper	
p FLAG-Zfyve26	This paper	
p FLAG-RAB11FIP5	This paper	
pGEX- GST-Rab5	This paper	
pGEX- GST-Rab11	This paper	
pGEX- GST-FIP3	This paper	
pGEX- GST-Rabep1	This paper	
Chemicals, peptides, and recombinant proteins		
Isopropyl β-D–thiogalactoside (IPTG)	Merck	Cat# I5502; RRID: AB_1079299
Glutathione	Thermofisher	Cat# 78259; RRID: AB_1079674
Glycerol	Merck	Cat# G5516; RRID: AB_1079203
Tris	Merck	Cat# T1503; RRID: AB_1079265
MgCl2	Merck	Cat# M8266; RRID: AB_1079241
NaCl	Merck	Cat# S5886; RRID: AB_1079281
PEI	Polysciences	Cat# 23966; RRID: AB_1080535
Triton X-100	Merck	Cat# T8787; RRID: AB_1079301
NaF	Merck	Cat# S7920; RRID: AB_1079283
Protease inhibitors cocktail	Roche	Cat# 11873580001; RRID: AB_1079257
GTPγS	Merck	Cat# G8634; RRID: AB_1079205
GDP	Merck	Cat# G7127; RRID: AB_1079201
Glutathione Agarose beads	Thermofisher	Cat# 16100; RRID: AB_1079675

(*Continued on next page*)

Continued

REAGENT or RESOURCE	SOURCE	IDENTIFIER
HEPES	Merck	Cat# H3375; RRID: AB_1079227
EDTA	Merck	Cat# E5134; RRID: AB_1079189
DTT	Merck	Cat# D0632; RRID: AB_1079185
Igepal CA-630	Merck	Cat# I3021; RRID: AB_1079231
Sodium orthovanadate	Merck	Cat# S6508; RRID: AB_1079277
Lipofectamine 2000	Thermofisher	Cat# 11668027; RRID: AB_1079680
Bovine Serum Albumin	Merck	Cat#: A9418-50G
CellMask Deep Red Actin	Thermofisher	Cat#: A57245; RRID: AB_2534021
Ammonium chloride	Merck	Cat#: 09718-250G
DAPI	Roche	Cat#: 10236276001; RRID: AB_2869624
Fluoromount-G	Thermofisher	Cat#: 00-4958-02
Human Transferrin	Merck	Cat#: T0665; RRID: AB_2337049
Alexa Fluor 647-conjugated human transferrin	Thermofisher	Cat#: T23366; RRID: AB_2337114
Glycine	VWR Life Science	Cat# M103-1KG
DMSO	Merck	Cat#: D8418
VPS34-IN1	Merck	Cat#: 5.32628
Paraformaldehyde	Thermofisher	Cat#: J61899.AK
Deposited data		
Mathematical models	Code Ocean	https://doi.org/10.24433/CO.5317183.v1
Tima lapse analysis	Code Ocean	https://doi.org/10.24433/CO.9194314.v1
Additional imaging analysis	Code Ocean	https://doi.org/10.24433/CO.3851388.v1
Experimental models: Cell lines		
HEK293T	ATCC	Cat# CRL-3216; RRID: CVCL_0063
COS7	ATCC	Cat# CRL-1651; RRID: CVCL_0224
U251-MG	ECACC	Cat# 09063001; RRID: CVCL_0021
Software and algorithms		
ImageJ	NIH	ImageJ
Julia programming language	GitHub	The Julia Programming Language
MATLAB	MathWorks	MATLAB - Il linguaggio del calcolo tecnico
CellProfiler	GitHub	CellProfiler · GitHub
Icy	Institute Pasteur, France Bioimaging	– Open Source Image Processing Software
Leica Application Suite X	Leica Software	LAS X Life Science Microscope Software - Downloads | Products | Leica Microsystems
GraphPad	GraphPad Prism	Home - GraphPad
Mathematical models algorithms	This paper	https://doi.org/10.24433/CO.5317183.v1
Algorithms for time lapse analysis	This paper	https://doi.org/10.24433/CO.9194314.v1
Algorithms for image analysis	This paper	https://doi.org/10.24433/CO.3851388.v1

EXPERIMENTAL MODEL AND STUDY PARTICIPANT DETAILS

Cell culture

In the following study we used U251MG cells (Homo sapiens, male, malignant glioblastoma, 75 years old, caucasian, diploid) purchased from ECACC repository (09063001), Cos-7 (Chlorocebus aethiops, male, adult, transformed by an origin-defective mutant of SV40 T-antigen) and 293T (Homo sapiens, kidney; embryo, transformed by SV40 T-antigen) cells obtained from ATCC catalog (ATCC CRL-1651, ATCC CRL-3216). All cell lines used in this study were cultured in DMEM supplemented with 10% FBS and kept in a humidified incubator at 37°C and 5% CO_2. The cell lines have not been authenticated. The cell lines were monthly tested for absence of mycoplasma.

METHOD DETAILS

Computational models

We generated 16 different competition-based models (I-XVI) in which each Rab species (i.e., RabX, RabY) forms a complex with the effector (i.e., E) and is associated to either a pFBL, a nFBL, a cFFL or an iFFL mediated by the shared effector. In parallel, we generated 16 different cascade-like models (XVII-XXXII) in which only one Rab species forms a complex with the effector and is associated to either a pFBL, a nFBL, a cFFL or a iFFL mediated by the effector E, whereas the other Rab is either positively (pR) or negatively (nR) regulated by the former complex. These different models are resumed below.

Model	Mechanism	*RabX* Regulation	*RabY* Regulation	Rab-effector interaction
I	Competition	pFBL	pFBL	$RabX^{GTP}_{Mem} : E, RabY^{GTP}_{Mem} : E$
II	Competition	pFBL	nFBL	$RabX^{GTP}_{Mem} : E, RabY^{GTP}_{Mem} : E$
III	Competition	pFBL	cFFL	$RabX^{GTP}_{Mem} : E, RabY^{GDP}_{Mem} : E$
IV	Competition	pFBL	iFFL	$RabX^{GTP}_{Mem} : E, RabY^{GDP}_{Mem} : E$
V	Competition	nFBL	pFBL	$RabX^{GTP}_{Mem} : E, RabY^{GTP}_{Mem} : E$
VI	Competition	nFBL	nFBL	$RabX^{GTP}_{Mem} : E, RabY^{GTP}_{Mem} : E$
VII	Competition	nFBL	cFFL	$RabX^{GTP}_{Mem} : E, RabY^{GDP}_{Mem} : E$
VIII	Competition	nFBL	iFFL	$RabX^{GTP}_{Mem} : E, RabY^{GDP}_{Mem} : E$
IX	Competition	cFFL	pFBL	$RabX^{GDP}_{Mem} : E, RabY^{GTP}_{Mem} : E$
X	Competition	cFFL	nFBL	$RabX^{GDP}_{Mem} : E, RabY^{GTP}_{Mem} : E$
XI	Competition	cFFL	cFFL	$RabX^{GDP}_{Mem} : E, RabY^{GDP}_{Mem} : E$
XII	Competition	cFFL	iFFL	$RabX^{GDP}_{Mem} : E, RabY^{GDP}_{Mem} : E$
XIII	Competition	iFFL	pFBL	$RabX^{GDP}_{Mem} : E, RabY^{GTP}_{Mem} : E$
XIV	Competition	iFFL	nFBL	$RabX^{GDP}_{Mem} : E, RabY^{GTP}_{Mem} : E$
XV	Competition	iFFL	cFFL	$RabX^{GDP}_{Mem} : E, RabY^{GDP}_{Mem} : E$
XVI	Competition	iFFL	iFFL	$RabX^{GDP}_{Mem} : E, RabY^{GDP}_{Mem} : E$
XVII	Cascade	pFBL	pR	$RabX^{GTP}_{Mem} : E$
XVIII	Cascade	pFBL	nR	$RabX^{GTP}_{Mem} : E$
XIX	Cascade	nFBL	pR	$RabX^{GTP}_{Mem} : E$
XX	Cascade	nFBL	nR	$RabX^{GTP}_{Mem} : E$
XXI	Cascade	cFFL	pR	$RabX^{GDP}_{Mem} : E$
XXII	Cascade	cFFL	nR	$RabX^{GDP}_{Mem} : E$
XXIII	Cascade	iFFL	pR	$RabX^{GDP}_{Mem} : E$
XXIV	Cascade	iFFL	nR	$RabX^{GDP}_{Mem} : E$
XXV	Cascade	pR	pFBL	$RabY^{GTP}_{Mem} : E$
XXVI	Cascade	nR	pFBL	$RabY^{GTP}_{Mem} : E$
XXVII	Cascade	pR	nFBL	$RabY^{GTP}_{Mem} : E$
XXVIII	Cascade	nR	nFBL	$RabY^{GTP}_{Mem} : E$
XXIX	Cascade	pR	cFFL	$RabY^{GDP}_{Mem} : E$
XXX	Cascade	nR	cFFL	$RabY^{GDP}_{Mem} : E$
XXXI	Cascade	pR	iFFL	$RabY^{GDP}_{Mem} : E$
XXXII	Cascade	nR	iFFL	$RabY^{GDP}_{Mem} : E$

In all competitive models (i.e., I-XVI) the two GTPases RabX and RabY bind to the molecular effector E. However, the models differ in which Rab form (GDP- or GTP-bound) binds to the effector E and in the type of control loops employed. Instead, in all cascade-like models (i.e., XVII-XXXII) only one GTPase binds to the effector E, either in its GDP or GTP-bound form. The set of possible reactions for the two Rab species, RabX and RabY, is given by:

$$RabX^{GDP}_{Cyt} \underset{k_{outX}}{\overset{k_{inX}}{\rightleftarrows}} RabX^{GDP}_{Mem}; \; RabY^{GDP}_{Cyt} \underset{k_{outY}}{\overset{k_{inY}}{\rightleftarrows}} RabY^{GDP}_{Mem}$$

$$RabX^{GDP}_{Mem} \underset{k_{GAPX}}{\overset{k_{GEFX}}{\rightleftarrows}} RabX^{GTP}_{Mem};\ RabY^{GDP}_{Mem} \underset{k_{GAPY}}{\overset{k_{GEFY}}{\rightleftarrows}} RabY^{GTP}_{Mem}$$

$$RabX^{GDP}_{Mem} + E \underset{k_{DX}}{\overset{k_{AX}}{\rightleftarrows}} RabX^{GDP}_{Mem} : E;\ RabY^{GDP}_{Mem} + E \underset{k_{DY}}{\overset{k_{AY}}{\rightleftarrows}} RabY^{GDP}_{Mem} : E$$

$$RabX^{GTP}_{Mem} + E \underset{k_{DX'}}{\overset{k_{AX'}}{\rightleftarrows}} RabX^{GTP}_{Mem} : E;\ RabY^{GTP}_{Mem} + E \underset{k_{DY'}}{\overset{k_{AY'}}{\rightleftarrows}} RabY^{GTP}_{Mem} : E$$

Inactive Rab GTPases (Rab^{GDP}) are represented both in their cytosolic ($RabX^{GDP}_{Cyt}$ and $RabY^{GDP}_{Cyt}$) and membrane-bound counterpart ($RabX^{GDP}_{Mem}$ and $RabY^{GDP}_{Mem}$). The conversion of $RabX^{GDP}_{Cyt}$ ($RabY^{GDP}_{Cyt}$) into $RabX^{GDP}_{Mem}$ ($RabY^{GDP}_{Mem}$) and vice versa, representing the shuttling between the cytoplasm and the endocytic membrane, is described by k_{inX} (k_{inY}) and k_{outX} (k_{outY}) rates, respectively. In contrast, active Rab forms are restricted to the membrane ($RabX^{GTP}_{Mem}$ and $RabY^{GTP}_{Mem}$), in accordance with previous reports.[44] Nucleotide exchange and hydrolysis of Rab small GTPases are described by rates k_{GEFX} (k_{GEFY}) and k_{GAPX}.(k_{GAPY}). $RabX^{GDP}_{Mem} : E$ and $RabY^{GDP}_{Mem} : E$ represent molecular complexes formed by the inactive GTPase forms and the effector, with k_{AX} and k_{AY} describing the rates of complex formation, whereas k_{DX} and k_{DY} representing dissociation rates. Analogously, $RabX^{GTP}_{Mem} : E$ and $RabY^{GTP}_{Mem} : E$ represent molecular complexes formed by the active GTPase forms and the effector, with $k_{AX'}$ and $k_{AY'}$ describing the rates of complex formation, whereas $k_{DX'}$ and $k_{DY'}$ representing dissociation rates. The general ODE system for the two GTPases, shared by all models, is given by:

$$\begin{cases}
\dfrac{d\left[RabX^{GDP}_{Cyt}\right]}{dt} = k_{outX}\left[RabX^{GDP}_{Mem}\right] - k_{inX}\left[RabX^{GDP}_{Cyt}\right] \\
\dfrac{d\left[RabX^{GDP}_{Mem}\right]}{dt} = k_{inX}\left[RabX^{GDP}_{Cyt}\right] - k_{outX}\left[RabX^{GDP}_{Mem}\right] + k_{GAPX}\left[RabX^{GTP}_{Mem}\right] - k_{GEFX}\left[RabX^{GDP}_{Mem}\right] + \\
\qquad - k_{AX}\left[RabX^{GDP}_{Mem}\right][E] + k_{DX}\left[RabX^{GDP}_{Mem} : E\right] \\
\dfrac{d\left[RabX^{GTP}_{Mem}\right]}{dt} = k_{GEFX}\left[RabX^{GDP}_{Mem}\right] - k_{GAPX}\left[RabX^{GTP}_{Mem}\right] - k_{AX'}\left[RabX^{GTP}_{Mem}\right][E] + k_{DX'}\left[RabX^{GTP}_{Mem} : E\right] \\
\dfrac{d\left[RabX^{GDP}_{Mem} : E\right]}{dt} = k_{AX}\left[RabX^{GDP}_{Mem}\right][E] - k_{DX}\left[RabX^{GDP}_{Mem} : E\right] \\
\dfrac{d\left[RabX^{GTP}_{Mem} : E\right]}{dt} = k_{AX'}\left[RabX^{GTP}_{Mem}\right][E] - k_{DX'}\left[RabX^{GTP}_{Mem} : E\right] \\
[RabX_{Tot}] = \left[RabX^{GDP}_{Cyt}\right] + \left[RabX^{GDP}_{Mem}\right] + \left[RabX^{GTP}_{Mem}\right] + \left[RabX^{GDP}_{Mem} : E\right] + \left[RabX^{GTP}_{Mem} : E\right] \\
\dfrac{d\left[RabY^{GDP}_{Cyt}\right]}{dt} = k_{outY}\left[RabY^{GDP}_{Mem}\right] - k_{inY}\left[RabY^{GDP}_{Cyt}\right] \\
\dfrac{d\left[RabY^{GDP}_{Mem}\right]}{dt} = k_{inY}\left[RabY^{GDP}_{Cyt}\right] - k_{outY}\left[RabY^{GDP}_{Mem}\right] + k_{GAPY}\left[RabY^{GTP}_{Mem}\right] - k_{GEFY}\left[RabY^{GDP}_{Mem}\right] + \\
\qquad - k_{AY}\left[RabY^{GDP}_{Mem}\right][E] + k_{DY}\left[RabY^{GDP}_{Mem} : E\right] \\
\dfrac{d\left[RabY^{GTP}_{Mem}\right]}{dt} = k_{GEFY}\left[RabY^{GDP}_{Mem}\right] - k_{GAPY}\left[RabY^{GTP}_{Mem}\right] - k_{AY'}\left[RabY^{GTP}_{Mem}\right][E] + k_{DY'}\left[RabY^{GTP}_{Mem} : E\right] \\
\dfrac{d\left[RabY^{GDP}_{Mem} : E\right]}{dt} = k_{AY}\left[RabY^{GDP}_{Mem}\right][E] - k_{DY}\left[RabY^{GDP}_{Mem} : E\right] \\
\dfrac{d\left[RabY^{GTP}_{Mem} : E\right]}{dt} = k_{AY'}\left[RabY^{GTP}_{Mem}\right][E] - k_{DY'}\left[RabY^{GTP}_{Mem} : E\right] \\
[RabY_{Tot}] = \left[RabY^{GDP}_{Cyt}\right] + \left[RabY^{GDP}_{Mem}\right] + \left[RabY^{GTP}_{Mem}\right] + \left[RabY^{GDP}_{Mem} : E\right] + \left[RabY^{GTP}_{Mem} : E\right] \\
\dfrac{d[E]}{dt} = k_{DX}\left[RabX^{GDP}_{Mem} : E\right] - k_{AX}\left[RabX^{GDP}_{Mem}\right][E] + k_{DX'}\left[RabX^{GTP}_{Mem} : E\right] - k_{AX'}\left[RabX^{GTP}_{Mem}\right][E] + \\
\qquad + k_{DY}\left[RabY^{GDP}_{Mem} : E\right] - k_{AY}\left[RabY^{GDP}_{Mem}\right][E] + k_{DY'}\left[RabY^{GTP}_{Mem} : E\right] - k_{AY'}\left[RabY^{GTP}_{Mem}\right][E]
\end{cases}$$

Each competitive and cascade-like model is obtained from this shared system. The distinct regulatory loops are implemented by appropriately modeling rate constants of interaction with the effector as follows.

1. If the effector interacts with *RabX* in its GTP-bound form, its rates relative to the $RabX^{GDP}_{Mem} : E$ complex formation and dissociation, k_{AX} and k_{DX}, are set to zero:

$$k_{AX} = k_{DX} = 0$$

Similarly, if the effector interacts with *RabY* in its GTP-bound form, its rates relative to the $RabY^{GDP}_{Mem} : E$ complex formation and dissociation, k_{AY} and k_{DY}, are set to zero:

$$k_{AY} = k_{DY} = 0$$

2. If conversely the effector interacts with *RabX* in its GDP-bound form, rate constants relative to the $RabX^{GTP}_{Mem} : E$ complex formation and dissociation, $k_{AX'}$ and $k_{DX'}$' are set to zero:

$$k_{AX'} = k_{DX'} = 0$$

Similarly, if the effector interacts with *RabY* in its GDP-bound form, its rates relative to the $RabY^{GTP}_{Mem} : E$ complex formation and dissociation, $k_{AY'}$ and $k_{DY'}$ are set to zero:

$$k_{AY'} = k_{DY'} = 0$$

3. If, instead, the effector does not directly interact with *RabX*, rate constants relative to both $RabX^{GDP}_{Mem} : E$ and $RabX^{GTP}_{Mem} : E$ complexes, k_{AX}, k_{DX}, $k_{AX'}$, and $k_{DX'}$ will be set to zero:

$$k_{AX} = k_{DX} = k_{AX'} = k_{DX'} = 0$$

Similarly, for *RabY*, if the effector does not directly interact with the GTPase, rate constants relative to both $RabY^{GDP}_{Mem} : E$ and $RabY^{GTP}_{Mem} : E$ complexes, k_{AY}, k_{DY}, $k_{AY'}$, and $k_{DY'}$ will be set to zero:

$$k_{AY} = k_{DY} = k_{AY'} = k_{DY'} = 0$$

4. A positive feedback loop acting on *RabX* is implemented by defining the *RabX* nucleotide exchange rate k_{GEFX} as a Hill function of the amount of $RabX^{GTP}_{Mem} : E$ complex, and keeping instead its hydrolysis rate equal to its constant basal value:

$$k_{GEFX} = k_{GEFbX} + k_{GEFMAXX}\frac{\left(RabX^{GTP}_{Mem} : E\right)^2}{\left(RabX^{GTP}_{Mem} : E\right)^2 + {k_{GEFMX}}^2}, k_{GAPX} = k_{GAPbX}$$

where k_{GEFbX} is the basal nucleotide exchange rate, k_{GEFMX} is the Michaelis-Menten constant and $k_{GEFMAXX}$ is the maximal effector-mediated nucleotide exchange rate. k_{GAPbX} represents the basal nucleotide exchange rate.

Similarly, a positive feedback loop acting on *RabY* is implemented by defining k_{GEFY} as a Hill function of the amount of $RabY^{GTP}_{Mem} : E$ complex, and keeping its hydrolysis rate constant:

$$k_{GEFY} = k_{GEFbY} + k_{GEFMAXY}\frac{\left(RabY^{GTP}_{Mem} : E\right)^2}{\left(RabY^{GTP}_{Mem} : E\right)^2 + {k_{GEFMY}}^2}, k_{GAPY} = k_{GAPbY}$$

where k_{GEFbY} is the basal nucleotide exchange rate, k_{GEFMY} is the Michaelis-Menten constant and $k_{GEFMAXY}$ is the maximal effector-mediated nucleotide exchange rate. k_{GAPbY} represents the basal nucleotide exchange rate.

5. A negative feedback loop acting on *RabX* is modeled by defining the *RabX* hydrolysis rate as a Hill function of the amount of $RabX^{GTP}_{Mem} : E$ complex and keeping its nucleotide exchange rate constant and equal to the basal value:

$$k_{GAPX} = k_{GAPbX} + k_{GAPMAXX}\frac{\left(RabX^{GTP}_{Mem} : E\right)^2}{\left(RabX^{GTP}_{Mem} : E\right)^2 + {k_{GAPMX}}^2}, k_{GEFX} = k_{GEFbX}$$

where k_{GAPbX} is the basal hydrolysis rate, k_{GAPMX} is the Michaelis-Menten constant and $k_{GAPMAXX}$ is the maximal effector-mediated hydrolysis rate. k_{GEFbX} represents the basal nucleotide exchange rate.

Similarly, a negative feedback loop acting on *RabY* is modeled by defining the *RabY* hydrolysis rate as a Hill function of the amount of $RabY^{GTP}_{Mem} : E$ complex and keeping its nucleotide exchange rate constant and equal to the basal value:

$$k_{GAPY} = k_{GAPbY} + k_{GAPMAXY}\frac{\left(RabY^{GTP}_{Mem} : E\right)^2}{\left(RabY^{GTP}_{Mem} : E\right)^2 + {k_{GAPMY}}^2}, k_{GEFY} = k_{GEFbY}$$

where k_{GAPbY} is the basal hydrolysis rate, k_{GAPMY} is the Michaelis-Menten constant and $k_{GAPMAXY}$ is the maximal effector-mediated hydrolysis rate. k_{GEFbY} represents the basal nucleotide exchange rate.

6. A coherent feedforward loop acting on *RabX* is modeled by defining the *RabX* nucleotide exchange rate as a Hill function of the amount of $RabX^{GDP}_{Mem}$ complex, and keeping instead its hydrolysis rate constant equal to the basal value:

$$k_{GEFX} = k_{GEFbX} + k_{GEFMAXX}\frac{\left(RabX^{GDP}_{Mem} : E\right)^2}{\left(RabX^{GDP}_{Mem} : E\right)^2 + {k_{GEFMX}}^2}, k_{GAPX} = k_{GAPbX}$$

where k_{GEFbX} is the basal nucleotide exchange rate, k_{GEFMX} is the Michaelis-Menten constant and $k_{GEFMAXX}$ is the maximal effector-mediated nucleotide exchange rate. k_{GAPbX} represents the basal nucleotide exchange rate.

Similarly, a coherent feedforward loop acting on *RabY* is modeled by defining the *RabY* nucleotide exchange rate as a Hill function of the amount of $RabY^{GDP}_{Mem}$ complex, and keeping instead its hydrolysis rate equal to its constant basal value:

$$k_{GEFY} = k_{GEFbY} + k_{GEFMAXY}\frac{\left(RabY^{GDP}_{Mem} : E\right)^2}{\left(RabY^{GDP}_{Mem} : E\right)^2 + {k_{GEFMY}}^2}, k_{GAPY} = k_{GAPbY}$$

where k_{GEFbY} is the basal nucleotide exchange rate, k_{GEFMY} is the Michaelis-Menten constant and $k_{GEFMAXY}$ is the maximal effector-mediated nucleotide exchange rate. k_{GAPbY} represents the basal nucleotide exchange rate.

7. An incoherent feedforward loop acting on *RabX* is modeled by defining the *RabX* hydrolysis rate as a Hill function of the amount of $RabX^{GDP}_{Mem} : E$ complex and keeping its nucleotide exchange rate instead equal to its constant basal value:

$$k_{GAPX} = k_{GAPbX} + k_{GAPMAXX}\frac{\left(RabX^{GDP}_{Mem} : E\right)^2}{\left(RabX^{GDP}_{Mem} : E\right)^2 + {k_{GAPMX}}^2}, k_{GEFX} = k_{GEFbX}$$

where k_{GAPbX} is the basal hydrolysis rate, k_{GAPMX} is the Michaelis-Menten constant and $k_{GAPMAXX}$ is the maximal effector-mediated hydrolysis rate. k_{GEFbX} represents the basal nucleotide exchange rate.

Similarly, an incoherent feedforward loop acting on *RabY* is modeled by defining the *RabY* hydrolysis rate as a Hill function of the amount of $RabY^{GDP}_{Mem}$ complex and keeping its nucleotide exchange rate equal to its constant basal value:

$$k_{GAPY} = k_{GAPbY} + k_{GAPMAXY}\frac{\left(RabY^{GDP}_{Mem} : E\right)^2}{\left(RabY^{GDP}_{Mem} : E\right)^2 + {k_{GAPMY}}^2}, k_{GEFY} = k_{GEFbY}$$

where k_{GAPbY} is the basal hydrolysis rate, k_{GAPMY} is the Michaelis-Menten constant and $k_{GAPMAXY}$ is the maximal effector-mediated hydrolysis rate. k_{GEFbY} represents the basal nucleotide exchange rate.

8. A positive regulation by *RabX* acting on *RabY* is modeled by defining the *RabY* nucleotide exchange rate as a Hill function of the amount of complex formed by *RabX* and the effector – either $RabX^{GDP}_{Mem} : E$ or $RabX^{GTP}_{Mem} : E$ - and keeping the hydrolysis rate instead equal to its constant basal value:

$$k_{GEFY} = k_{GEFbY} + k_{GEFMAXY}\frac{\left(RabX^{GDP}_{Mem} : E\right)^2}{\left(RabX^{GDP}_{Mem} : E\right)^2 + {k_{GEFMY}}^2}, k_{GAPY} = k_{GAPbY}$$

or

$$k_{GEFY} = k_{GEFbY} + k_{GEFMAXY}\frac{\left(RabX_{Mem}^{GTP} : E\right)^2}{\left(RabX_{Mem}^{GTP} : E\right)^2 + {k_{GEFMY}}^2}, k_{GAPY} = k_{GAPbY}$$

where k_{GEFbY} is the basal nucleotide exchange rate, k_{GEFMY} is the Michaelis-Menten constant and $k_{GEFMAXY}$ is the maximal effector-mediated hydrolysis rate. k_{GAPbY} represents the basal hydrolysis rate.

Vice versa, a positive regulation by *RabY* acting on *RabX* is modeled by defining the *RabX* nucleotide exchange rate as a Hill function of the amount of complex formed by *RabY* and the effector – either $RabY_{Mem}^{GDP} : E$ or $RabY_{Mem}^{GTP} : E$ - and keeping the hydrolysis rate instead equal to its constant basal value:

$$k_{GEFX} = k_{GEFbX} + k_{GEFMAXX}\frac{\left(RabY_{Mem}^{GDP} : E\right)^2}{\left(RabY_{Mem}^{GDP} : E\right)^2 + {k_{GEFMX}}^2}, k_{GAPX} = k_{GAPbX}$$

or

$$k_{GEFX} = k_{GEFbX} + k_{GEFMAXX}\frac{\left(RabY_{Mem}^{GTP} : E\right)^2}{\left(RabY_{Mem}^{GTP} : E\right)^2 + {k_{GEFMX}}^2}, k_{GAPX} = k_{GAPbX}$$

where k_{GEFbX} is the basal nucleotide exchange rate, k_{GEFMX} is the Michaelis-Menten constant and $k_{GEFMAXX}$ is the maximal effector-mediated hydrolysis rate. k_{GAPbX} represents the basal hydrolysis rate.

9. A negative regulation by *RabX* acting on *RabY* is modeled by defining the *RabY* hydrolysis rate as a Hill function of the amount of complex formed by *RabX* and the effector – either $RabX_{Mem}^{GDP} : E$ or $RabX_{Mem}^{GTP}$ - and keeping the nucleotide exchange rate instead equal to its constant basal value:

$$k_{GAPY} = k_{GAPbY} + k_{GAPMAXY}\frac{\left(RabX_{Mem}^{GDP} : E\right)^2}{\left(RabX_{Mem}^{GDP} : E\right)^2 + {k_{GAPMY}}^2}, k_{GEFY} = k_{GEFbY}$$

or

$$k_{GAPY} = k_{GAPbY} + k_{GAPMAXY}\frac{\left(RabX_{Mem}^{GTP} : E\right)^2}{\left(RabX_{Mem}^{GTP} : E\right)^2 + {k_{GAPMY}}^2}, k_{GEFY} = k_{GEFbY}$$

where k_{GAPbY} is the basal hydrolysis rate, k_{GAPMY} is the Michaelis-Menten constant and $k_{GAPMAXY}$ is the maximal effector-mediated hydrolysis rate. k_{GEFbY} represents the basal nucleotide exchange rate.

Vice versa, a negative regulation by *RabY* acting on *RabX* is modeled by defining the *RabX* hydrolysis rate as a Hill function of the amount of complex formed by *RabY* and the effector – either $RabY_{Mem}^{GDP} : E$ or $RabY_{Mem}^{GTP}$- and keeping the nucleotide exchange rate instead equal to its constant basal value:

$$k_{GAPX} = k_{GAPbX} + k_{GAPMAXX}\frac{\left(RabY_{Mem}^{GDP} : E\right)^2}{\left(RabY_{Mem}^{GDP} : E\right)^2 + {k_{GAPMX}}^2}, k_{GEFX} = k_{GEFbX}$$

or

$$k_{GAPX} = k_{GAPbX} + k_{GAPMAXX}\frac{\left(RabY_{Mem}^{GTP} : E\right)^2}{\left(RabY_{Mem}^{GTP} : E\right)^2 + {k_{GAPMX}}^2}, k_{GEFX} = k_{GEFbX}$$

where k_{GAPbX} is the basal hydrolysis rate, k_{GAPMX} is the Michaelis-Menten constant and $k_{GAPMAXX}$ is the maximal effector-mediated hydrolysis rate. k_{GEFbX} represents the basal nucleotide exchange rate.

Thus, each model is obtained from the shared ODE system by setting rate constants as follow.

Model	k_{AX} k_{DX}	$k_{AX'}$ $k_{DX'}$	k_{AY} k_{DY}	$k_{AY'}$ $k_{DY'}$	k_{GEFX}	k_{GAPX}	k_{GEFY}	k_{GAPY}
I	0	$\neq 0$	0	$\neq 0$	Hill of $RabX_{Mem}^{GTP}$	basal	Hill of $RabY_{Mem}^{GTP}$	basal
II	0	$\neq 0$	0	$\neq 0$	Hill of $RabX_{Mem}^{GTP}$	basal	basal	Hill of $RabY_{Mem}^{GTP}$
III	0	$\neq 0$	$\neq 0$	0	Hill of $RabX_{Mem}^{GTP}$	basal	Hill of $RabY_{Mem}^{GDP}$	basal
IV	0	$\neq 0$	$\neq 0$	0	Hill of $RabX_{Mem}^{GTP}$	basal	basal	Hill of $RabY_{Mem}^{GDP}$

(*Continued on next page*)

Continued

Model	k_{AX} k_{DX}	$k_{AX'}$ $k_{DX'}$	k_{AY} k_{DY}	$k_{AY'}$ $k_{DY'}$	k_{GEFX}	k_{GAPX}	k_{GEFY}	k_{GAPY}
V	0	≠0	0	≠0	basal	Hill of $RabX^{GTP}_{Mem}$	Hill of $RabY^{GTP}_{Mem}$	basal
VI	0	≠0	0	≠0	basal	Hill of $RabX^{GTP}_{Mem}$	basal	Hill of $RabY^{GTP}_{Mem}$
VII	0	≠0	≠0	0	basal	Hill of $RabX^{GTP}_{Mem}$	Hill of $RabY^{GDP}_{Mem}$	basal
VIII	0	≠0	≠0	0	basal	Hill of $RabX^{GTP}_{Mem}$	basal	Hill of $RabY^{GDP}_{Mem}$
IX	≠0	0	0	≠0	Hill of $RabX^{GDP}_{Mem}$	basal	Hill of $RabY^{GTP}_{Mem}$	basal
X	≠0	0	0	≠0	Hill of $RabX^{GDP}_{Mem}$	basal	basal	Hill of $RabY^{GTP}_{Mem}$
XI	≠0	0	≠0	0	Hill of $RabX^{GDP}_{Mem}$	basal	Hill of $RabY^{GDP}_{Mem}$	Basal
XII	≠0	0	≠0	0	Hill of $RabX^{GDP}_{Mem}$	basal	basal	Hill of $RabY^{GDP}_{Mem}$
XIII	≠0	0	0	≠0	basal	Hill of $RabX^{GDP}_{Mem}$	Hill of $RabY^{GTP}_{Mem}$	Basal
XIV	≠0	0	0	≠0	basal	Hill of $RabX^{GDP}_{Mem}$	basal	Hill of $RabY^{GTP}_{Mem}$
XV	≠0	0	≠0	0	basal	Hill of $RabX^{GDP}_{Mem}$	Hill of $RabY^{GDP}_{Mem}$	Basal
XVI	≠0	0	≠0	0	basal	Hill of $RabX^{GDP}_{Mem}$	basal	Hill of $RabY^{GDP}_{Mem}$
XVII	≠0	0	0	0	Hill of $RabX^{GTP}_{Mem}$	basal	Hill of $RabX^{GTP}_{Mem}$	Basal
XVIII	≠0	0	0	0	Hill of $RabX^{GTP}_{Mem}$	basal	basal	Hill of $RabX^{GTP}_{Mem}$
XIX	≠0	0	0	0	basal	Hill of $RabX^{GTP}_{Mem}$	Hill of $RabX^{GTP}_{Mem}$	Basal
XX	≠0	0	0	0	basal	Hill of $RabX^{GTP}_{Mem}$	basal	Hill of $RabX^{GTP}_{Mem}$
XXI	0	≠0	0	0	Hill of $RabX^{GDP}_{Mem}$	basal	Hill of $RabX^{GDP}_{Mem}$	Basal
XXII	0	≠0	0	0	Hill of $RabX^{GDP}_{Mem}$	basal	basal	Hill of $RabX^{GDP}_{Mem}$
XXIII	0	≠0	0	0	basal	Hill of $RabX^{GDP}_{Mem}$	Hill of $RabX^{GDP}_{Mem}$	basal
XXIV	0	≠0	0	0	basal	Hill of $RabX^{GDP}_{Mem}$	basal	Hill of $RabX^{GDP}_{Mem}$
XXV	0	0	≠0	0	Hill of $RabY^{GTP}_{Mem}$	basal	Hill of $RabY^{GTP}_{Mem}$	basal
XXVI	0	0	≠0	0	basal	Hill of $RabY^{GTP}_{Mem}$	Hill of $RabY^{GTP}_{Mem}$	basal
XXVII	0	0	≠0	0	Hill of $RabY^{GTP}_{Mem}$	basal	basal	Hill of $RabY^{GTP}_{Mem}$
XXVIII	0	0	≠0	0	basal	Hill of $RabY^{GTP}_{Mem}$	basal	Hill of $RabY^{GTP}_{Mem}$
XXIX	0	0	0	≠0	Hill of $RabY^{GDP}_{Mem}$	basal	Hill of $RabY^{GDP}_{Mem}$	basal
XXX	0	0	0	≠0	basal	Hill of $RabY^{GDP}_{Mem}$	Hill of $RabY^{GDP}_{Mem}$	basal
XXXI	0	0	0	≠0	Hill of $RabY^{GDP}_{Mem}$	basal	basal	Hill of $RabY^{GDP}_{Mem}$
XXXII	0	0	0	≠0	basal	Hill of $RabY^{GDP}_{Mem}$	basal	Hill of $RabY^{GDP}_{Mem}$

These models were made available at Code Ocean: https://doi.org/10.24433/CO.5317183.v1.

Mathematical model parameter estimation

Baseline parameter values were set according to the orders of magnitude known in literature. The basal Rab5 GEF activity rate was found to be of the order 10^{-2} s^{-1} *in vitro*,[45] whereas the analogous rate value for Rab11 is missing. We thus set the basal GDP/GTP exchange rate of both RabX and RabY, k_{GEFbX} and k_{GEFbY}, to 10^{-2} s^{-1}. Despite rate constants associated to effector-mediated Rab activation are largely unknown, the rate of Rab5 activation catalyzed by the Rabex-5-Rabaptin-5 complex was measured to be of the order 10^{-2} s^{-1} *in vitro*.[38] Thus, the maximum values of Hill functions implementing effector-mediated activation of RabX and RabY, $k_{GEFMAXX}$ and $k_{GEFYMAXY}$, were set to this value.

A value of 10^{-2} s^{-1} was measured for Rab5 basal hydrolysis rate,[46] while the counterpart for Rab11 is lacking. We thereby set k_{GAPbX} and k_{GAPbY} to 10^{-2} s^{-1}. Similarly, due to the lack of effector-mediated Rab deactivation rate values, we set the maximum values of the Hill functions, $k_{GAPXMAX}$ and $k_{GAPYMAX}$, to the same value of basal hydrolysis rate, that is to 10^{-2} s^{-1}.

Remaining parameters relative to Hill functions were set by choosing realistic orders of magnitude: Michaelis-Menten constants of Hill functions, representing half of the amount of GTPase-effector complex required to reach maximum feedback rates, were all set to the same arbitrary value of 50 molecules. Exponents of activatory Hill functions were set to $n = 2$ in order to account for cooperativity in the feedback mechanism, as it has been proposed that effector-mediated GEF recruitment leads to cooperative Rab activation.[6] For symmetry, exponents of Hill functions describing negative feedbacks were set to the same value $n_X = n_Y = 2$.

The rate of Rab5 membrane binding was measured to be of the order of 10^{-2} s^{-1} *in vitro*.[47] We thereby set both parameters k_{inX} and k_{inY} to 10^{-2} s^{-1}. Since precise kinetic measurements of GDI-mediated Rab membrane extraction are still lacking, we set rates k_{outX} and k_{outY} to the same baseline value of 10^{-2} s^{-1}.

Rates of Rab-effector complex formation and dissociation involving either active or inactive GTPase forms were set for both RabX and RabY to the same arbitrary value: $k_{AX} = k_{DX} = k_{AX'} = k_{DX'} = k_{AY} = k_{DY} = k_{AY'} = k_{DY'} = 10^{-3}$.

Parameter	Value (1/s)
k_{inX}; k_{outX}; k_{inY}; k_{outY}	0.01
k_{GEFbX}; k_{GAPbX}; k_{GEFbY}; k_{GAPbY}	0.01
$k_{GEFMAXX}$; $k_{GAPMAXX}$; $k_{GEFMAXY}$; $k_{GAPMAXY}$	0.01
k_{GEFMX}; k_{GAPMX}; k_{GEFMY}; k_{GAPMY}	50
k_{AX}; k_{DX}; k_{AY}; k_{DY}	0.001
$k_{AX'}$; $k_{DX'}$; $k_{AY'}$; $k_{DY'}$	0.001
n_X; n_y	2

Cell transfection

Cos-7 cells were transfected with plasmids encoding fluorescent version of Rab5 and Rab11 proteins using Lipofectamine 2000 (Invitrogen) according to the manufacturer's protocol. 293T cells were transfected using PEI (Polysciences 23966) according to the manufacturer's protocol.

Antibodies

The following primary antibodies were used in this study: rabbit-*anti*-Rab11 (Cell Signaling (D4F5) 5589, immunofluorescence (IF) 1:100); mouse-*anti*-Rab5 (BD Biosciences 610725, IF 1:100); mouse-*anti*-PI(3)P (Echelon Biosciences Z-P003, IF 1:300), mouse-*anti*-Rab11 (BD Biosciences 610656, western blot (WB) 1:1000), mouse-*anti*-Rab5A (Cell Signaling (E6N8S) 46449, WB 1:1000), mouse anti-GFP (Cell Signaling (4B10) 2955, WB, 1:1000) mouse-*anti*-GAPDH (Proteintech 60004-1, WB, 1; 5000).

The following secondary antibodies were used in this study: anti-mouse/rabbit IgG Atto 488 (Sigma-Aldrich 18772, IF 1:200); anti-mouse IgG 550 Atto (Sigma-Aldrich 43394, IF 1:200); anti-rabbit IgG 647 Alexa-Fluor (Invitrogen A32733TR, 1:400), Anti-Mouse IgG HRP (Sigma-Aldrich A4416 1:500/1000), Anti-Rabbit IgG HRP (Sigma-Aldrich A6154, 1:500/1000).

Plasmids

Plasmids encoding Zfyve26[30] protein and Rab5 FRET biosensor (Raichu-Rab5)[27] were kindly provided by prof. Christian Hübner (Institute of Human Genetics, University Hospital, Jena, Germany) and Michiyuki Matsuda (Department of Pathology and Biology of Diseases, Graduate School of Medicine, Kyoto University, Japan) respectively. Plasmid encoding Rab11 FRET biosensor (AS-Rab11) [28] mEGFP, mEGFP-Rab5 (and its variants), mEGFP-Rab11 (and its variants) were kindly provided by Prof. Emilio Hirsch (Department of Molecular Biotechnology and Health Sciences, University of Turin, Italy). Plasmid encoding mCherry, mCherry-Rab11a, mCherry-Rab5 (and its variants), FLAG-Zfyve26, FLAG-RAB11FIP5 were generated by PCR and restriction enzyme cloning.

Time-lapse microscopy

5x10^4 Cos-7 cells were plated in 8 well μ-Slide imaging dishes (Ibidi) and transfected with the indicated proteins combinations: i) Raichu-Rab5 and mCherry-Rab11a, ii) Raichu-Rab5, mCherry-Rab11a, and Zfyve26-FLAG, iii) Raichu-Rab5, mCherry-Rab11a and FLAG-Rab11FIP5, iv) As-Rab11 and mCherry-Rab5, v) As-Rab11 and mCherry-Rab5 and Zfyve26-FLAG or, vi) As-Rab11 and mCherry-Rab5 and FLAG-Rab11FIP5. After 48 h, cells were starved for 2 h in serum-free DMEM 0.1% BSA at 37°C in 5% CO2. Human Transferrin was added at a concentration of 20 μg/ml for the time of the acquisition. Imaging was performed in a CO2 independent medium, Dulbecco's modified Eagle's medium without FBS (Invitrogen, 61965026). Time-lapse series were acquired at 37°C on an inverted confocal Leica SP8 microscope with AOBS equipped with 63× O2/Oil immersion objective, NA 1.40. The temperature was controlled by a climate box covering the set up. Fluorescent tagged proteins were imaged sequentially in line-interlace mode to eliminate cross-talk between the channels. mECFP was excited with a 458-nm laser line and imaged at 470–500-nm bandpass emission filters. mcpVenus/YFP was excited with the 514-nm argon laser line and imaged through a 525–550-nm bandpass emission filter. mCherry/mRFP was excited with the 568-nm helium neon laser line and imaged through a 580–650-nm bandpass emission filter. Serial sections were acquired satisfying the Nyquist criterion. Acquisition was performed at zoom (×40) in a region of 4.6 μm in side. The ROI (Region Of Interest) has been chosen to contain the endosome and the surrounding intracellular region. Exposure times and readout were fixed for a resulting time-lapse sequence of roughly one frame every 150 ms. Images obtained were stacked and exported as a single TIFF file.

Time lapse image processing

An image segmentation code for the identification of the endosomal surface, our region of interest (ROI), based on the fluorescence intensity of Rab5 probe was developed using the MATLAB R2023a software (MathWorks, MA, USA) integrated with Image Processing and Bio-formats Toolbox. A matrix of 128X128 pixels containing intensity values was generated for each fluorescent signal (e.g., mECFP, mcpVENUS/YFP, mCherry, FRET sensitized). After background subtraction and maximum projection of the Rab5 signal (YFP emission channel) (max function) a linear contrast was applied (imadjust function) and noise was reduced by Gaussian smoothing (fspecial Gaussian option). Next, the matrix was converted to grayscale (mat2gray function). A custom threshold was fixed for

image conversion to binary (im2bw function). Generated ring-shaped components were closed by subsequent dilatation and erosion of the identified region (imclose function) with custom parameters. Endosome identification was improved by discarding: i) objects smaller than the largest connected component, ii) objects showing: up near frame boundaries, iii) objects that do not satisfy a minimum of 0.6 "rotundity" index - calculated as $p^2/4\pi a$, where p indicates the object's perimeter and a indicates its area – taking value 1 if an object is perfectly round.

The accuracy of this segmentation procedure was manually evaluated for each frame composing time-lapse video. Frames that show identification errors after were not considered for the final ROI identification. Next, to obtain a single ROI representing the endosome surface throughout the timelapse, an average endosomal lumen was computed by identifying, aligning framewise centroids to a common constant point, and subsequently averaging framewise aligned endosomes and converting such average object to binary using a customized threshold. Lastly, the ROI representing the endosome surface was obtained by applying a ring-shaped mask with a thickness of 15 pixels built surrounding the endosomal lumen. For each frame, the obtained ring-shaped ROI was applied identically, and pixels not included were forced to zero values.

Also, pixels with negative fluorescence were forced to zero values. Similarly, ECFP and FRET sensitized signals were forced to zero in pixels where mcpVenus/YFP fluorescence was absent. FRET ratio values were calculated by adapting previous protocols.[48] To avoid generation of artifacts in FRET ratio calculation due to overscale sensitized FRET values, only signals exceeding the highest 50% of ROI FRET sensitized data were used. Next, using the new sensitized FRET image, the FRET ratio image was obtained by computing the FRET to ECFP ratio. These scripts were made available at Code Ocean: https://doi.org/10.24433/CO.9194314.v1.

FRAP analysis

FRAP experiments were performed in FluoroBrite DMEM media (Invitrogen, A18967-01) supplemented with 4 mM L-glutamine at 37°C, 5% CO2. Time-lapse series were acquired by inverted confocal Leica SP8 microscope with AOBS equipped with 40x Oil immersion objective, NA 1.25. The temperature was controlled by a climate box covering the set up. One spheric-like endosome positive to GFP-Zfyve26 was bleached by using a 488 nm argon laser at 80% of full power (8 iterations), and the recovery was monitored over 3 min by scanning the whole cell at 1 s interval for the first 15 frames and at 3 s for the remaining part of the acquisition.

Post-bleaching fluorescence intensity was determined by Leica Application Suite X (LAS X) software. Data obtained were background subtracted, normalized, and corrected for bleaching.[49]

Immunofluorescence

Cos-7 cells were plated onto sterile 12 mm glass coverslips and fixed with 4% paraformaldehyde for 15 min after treatments (e.g., transferrin, VPS34-IN1 inhibitor). Cell were permeabilized (0.1% saponin in PBS) for 10 min, quenched (50 mM NH4Cl) for 10 min and blocked with 3% BSA in PBS for 1h. Coverslips were incubated in primary antibodies (e.g., anti-Rab5, anti-Rab11, anti-PI(3)P antibodies listed in the appropriate section) for 1 h and 30 min and washed three times in PBS followed by 30 min of incubation in fluorescently tagged secondary antibodies. After secondary antibodies incubation, coverslips were washed three times with PBS and stained with DAPI. For accurate image segmentation, both control and treated cells were stained with CellMask Deep Red Actin (Invitrogen, A57245) for 15 min before DAPI staining Coverslips were mounted onto glass slide using Fluoromount-G (Invitrogen, 00-4958-02), Images were taken by SPEII confocal microscope using a 40X/1.15 oil objective.

For transferrin stimulation experiments, cells were starved for 2 h in DMEM containing both 0.1% FBS and 0.1% BSA at 37°C. Then cells were stimulated with 20 μg/mL of human transferrin (Sigma, T0665) in DMEM containing both 0.1% FBS and 0.1% BSA for 30 min at 37°C and then fixed and stained as described before.

For PI(3)P inhibition experiments, cells were treated with either 0.1% DMSO (control condition) or VPS34-IN1 inhibitor (Merck, 532628) at 1 μM for 90 min, fixed and stained as described before.

Transferrin recycling assay

Cos-7 cells transiently expressing either GFP or GFP-Zfyve26 proteins were starved for 2 h in DMEM 0.1% FBS containing 0.1% BSA at 37°C, 5% CO2. Next, cells were treated with 20 μg/mL of Alexa Fluor 647-conjugated human transferrin (Invitrogen, T23366) in 0.1% FBS DMEM for 30 min at 37°C, 5% CO2. After 37°C PBS washing, cells were chased in complete DMEM medium containing 0.1% BSA for various length times at 37°C, 5% CO2. At each time point of interest, cells were washed twice with ice-cold PBS and acid stripping solution (100mM NaCl, 50 mM glycine, pH 4.5) was added for 1 min. Finally, cells were twice washed with ice-cold PBS, fixed in 4% paraformaldehyde followed by PBS washing and DAPI staining. Cells images were taken by SPEII confocal microscope using a 40X/1.15 oil objective, manually segmented by CellProfiler software (version 4.2.5)[50] and Mean Fluorescence Intensity was measured by a custom pipeline in MATLAB R2023a software (Mathworks, MA, USA). These scripts were made available at Code Ocean: https://doi.org/10.24433/CO.3851388.v1.

Recombinant protein production

Plasmids encoding GST-Rab5, GST-Rab11, GST-FIP3 (649–756) and GST-Rabep1 (738–862) were cloned in pGEX vectors and transformed in BL21 (DE3) for production protein. Protein expression was induced by addition of isopropyl β-D–thiogalactoside (IPTG, 1.0 mM) at room temperature for 6 h. Recombinant proteins were purified (elution 10 mM glutathione, PBS), dialyzed, frozen in liquid nitrogen, and stocked (50% glycerol in Tris–HCl 10 mM 5 mM MgCl2, 100 mM NaCl) at −80°C.

ZFYVE26 pull-down assay

HEK293T cells growing in 15-cm dishes were transfected with DNA mixtures containing 30 μg of pCMVTag2B or FLAG-Zfyve26, using PEI transfection reagent. After 48h, cells were harvested and homogenized in Lysis Buffer (20 mM Tris pH [8], 150 mM NaCl, 10 mM MgCl2, 1% Triton X-100, 10 mM NaF, EDTA-free protease inhibitors cocktail) and cleared by centrifugation.

In parallel, nucleotide-bound GST-RABs recombinant proteins either GTPγS- or GDP-loaded were generated by incubating 30 μg of recombinant GST-Rab11a or GST-Rab5a together with Glutathione Agarose beads (Thermofisher 16100) on a rotating rack for 1h at 4°C. Beads were washed 4 times with Buffer A (50 mM HEPES pH [7.6], 5 mM EDTA, 1 mM DTT) and incubated in Buffer A on a rotating rack for 2h at RT. Beads were washed 4 times with Loading Buffer (20 mM Tris pH [8], 150 mM NaCl, 5 mM EDTA, 1 mM DTT) and resuspended in Loading Buffer. GTPγS (Merck G8634) or GDP (Merck G7127) was added at a molar ratio 25:1 of GTPγS/GDP:Rab and samples were incubated on a rotating rack for 3h at RT. Beads were washed 4 times with and resuspended in Assay Buffer (20 mM Tris pH [8], 150 mM NaCl, 10 mM MgCl).

The clarified lysates were incubated together with GST-Rabs beads loaded with either GTPγS or GDP on a rotating rack for 2h at 4°C. Beads were washed 5 times with Lysis Buffer and resuspended in Laemmli buffer for SDS–PAGE and immunoblot analysis. For quantification analysis, pictures were taken ensuring that intensity was within the linear range and the Quantity One 1-D analysis software (Bio-Rad) was used.

Rab5 and Rab11-activation pull down assay

HEK293T cells growing in 10-cm dishes were transfected with DNA mixtures containing 10 μg of pCMVTag2B or 10 μg of FLAG-Zfyve26, using PEI transfection reagent. After 48h, cells were harvested and homogenized in lysis buffer (50 mM Tris-HCl pH [7.5], 150 mM NaCl, 1% Igepal CA-630, 10% glycerol, 25 mM NAF, 10 mM MgCl2, 1 mM EDTA, 1mM sodium orthovanadate, and protease inhibitor cocktail) and cleared by centrifugation. A total of 1 mg of protein extract was incubated with 25 μg of recombinant GST-Rabep1 or GST-Rab11FIP3 coupled with Glutathione Agarose beads (Thermofisher 16100) on a rotating rack for 2h at 4°C. Beads were washed 5 times with Lysis Buffer and resuspended in Laemmli buffer for SDS-PAGE and immunoblot analysis. Endogenous content of total Rab5 or Rab11 in cell lysates was measured by loading 10 μg of total extracts in a different gel followed by immunoblot and used to normalize measurements of active Rab5 and Rab11, respectively. For quantification analysis, pictures were taken ensuring that intensity was within the linear range and the Quantity One 1-D analysis software (Bio-Rad) was used.

QUANTIFICATION AND STATISTICAL ANALYSIS

Quantification of Mean Square Displacement

Mean square displacement (MSD) was calculated using Icy software (icy.bioimageanalysis.org). In brief, Spot Tracking plugin was used to segment and track Rab5-positive and Rab11-positive structures in time-lapse videos of cells transfected with Raichu-Rab5 and mCherry-Rab11a. Next, track Manager plugin in Icy software was used to compute the Mean Square Displacement over time of the structures previously segmented and tracked.

Quantification of the number of GFP-Zfyve26 structures

Cells transfected with GFP-Zfyve26 were treated with either DMSO/VPS34-IN1 inhibitor or vehicle/Transferrin. Then, they were fixed in PFA (4%) and imaged using an SPEII confocal microscope equipped with a 40X/1.15 oil objective. GFP-Zfyve26 was excited with a 488-nm laser line and emitted light was collected at 500–530 nm bandpass emission filters. Random sampling of the coverslip was performed by avoiding cells placed on the edges of the coverslip. For each sampled cell, we manually counted the number of GFP-Zfyve26 positive signals. This count included both spot and spherical GFP-Zfyve26 positive structures.

Quantification of cells with spherical endosomes

Cell treated with either Transferrin or vehicle were fixed in PFA (4%), immunostained for both Rab5 and Rab11 and imaged using an SPEII confocal microscope equipped with a 40X/1.15 oil objective (detailed procedure on the immunostaining labeling was provided in the paragraph entitled "immunofluorescence" of the STAR Methods section). Labeled Rab5 and Rab11 were excited with either 550-nm or 488 laser line and emitted light was collected using either 570–590 nm or 515–535 nm bandpass emission. Random sampling of the coverslip was performed by avoiding cells placed on the edges of the coverslip. We manually counted each cell displaying at least one spherical endosome positive for both Rab5 and Rab11. The number obtained from this count was divided by the total number of cells sampled.

Quantification of the number of Rab5/Rab11-positive structures for single cells

Cells transfected either for GFP (control) or GFP-Zfyve26 were fixed in PFA (4%), immunostained for both Rab5 and Rab11 and imaged using an SPEII confocal microscope equipped with a 40X/1.15 oil objective (detailed procedure on the immunostaining labeling was provided in the paragraph entitled "immunofluorescence" of the STAR Methods section). Image processing and segmentation was performed using CellProfiler software, while assignment of spot cell identity and computation of the number of Rab5/Rab11 positive structures were performed using MATLAB 2023a. In brief, manually identified cells were obtained using the "IdentifyObjectsManually" module and noise filtered using "MedianFilter" module contained in CellProfiler. Afterward, extraction and

automatic identification of both Rab5-and Rab11-fluorescent spots was performed using top-hat filtering and Otsu's thresholding method with adaptive threshold using ''EnhanceOrSuppressFeatures'' module and ''IdentifyPrimaryObjects'' module contained in CellProfiler software. These segmentation masks were loaded in a custom MATLAB script that assigned each fluorescent spot to the cell of origin and counted the resulting number of Rab5-and Rab11-positive structures per cell. These scripts were made available at Code Ocean: https://doi.org/10.24433/CO.3851388.v1.

Quantification of Rab5/Rab11 mean fluorescence intensity, area and separation

Cells transfected either for GFP (control) or GFP-Zfyve26 were fixed in PFA (4%), immunostained for both Rab5 and Rab11 and imaged using an SPEII confocal microscope equipped with a 40X/1.15 oil objective (detailed procedure on the immunostaining labeling was provided in the paragraph entitled ''immunofluorescence'' of the STAR Methods section). Image processing and segmentation was performed using CellProfiler software, while assignment of Rab5/Rab11-positive structures to the corresponding spherical endosome and the computation of Rab5/Rab11 mean fluorescence intensity, area and separation were performed using MATLAB 2023a. In brief, single spherical endosomes were manually identified using the ''IdentifyObjectsManually'' module, followed by noise reduction using the ''MedianFilter'' module contained in CellProfiler. Afterward, extraction and automatic identification of both Rab5-and Rab11-positive structures was performed using top-hat filtering and Otsu's thresholding method with adaptive threshold using ''EnhanceOrSuppressFeatures'' module and ''IdentifyPrimaryObjects'' module contained in CellProfiler software. Segmentation masks of single spherical endosomes and Rab5/Rab11-positive structures, along with images of Rab5 and Rab11 immunostaining were loaded in a custom MATLAB script. It assigned each Rab5/Rab11-positive structures to its corresponding spherical endosome and computed Rab5/Rab11 mean fluorescence intensity, area and separation. The area of both Rab5-and Rab11-positive structures was determined by multiplying the number of pixels in each structure by the area of a single pixel (110 nm × 110 nm). The Rab5-Rab11 separation was computed by 1 minus Mander's Coefficient. Mean fluorescence intensity was calculated by summing the pixel intensities of Rab5-or Rab11-positive structures and dividing by the total number of pixels in each structure. These scripts were made available at Code Ocean: https://doi.org/10.24433/CO.3851388.v1.

Quantification of the number of PI(3)P-positive structures and mean fluorescence intensity

Cell treated with either vehicle/Transferrin or DMSO/VPS34-IN1 were fixed in PFA (4%), immunostained for PI(3)P and imaged using an SPEII confocal microscope equipped with a 40X/1.15 oil objective (detailed procedure on the immunostaining labeling was provided in the paragraph entitled ''immunofluorescence'' of the STAR Methods section). Image processing and segmentation was performed using CellProfiler software, while assignment of PI(3)P-positive structures or pixel intensities to the corresponding cell, as well as the computation of PI(3)P mean fluorescence intensity and count per cell, were performed using MATLAB 2023a. In brief, single cells treated with either vehicle or Transferrin were manually identified using the ''IdentifyObjectsManually'' module. Afterward, noise reduction was performed by ''MedianFilter'' module, followed by extraction and automatic identification of PI(3)P-positive structures. This was achieved by top-hat filtering and Otsu's thresholding method with adaptive threshold, using ''EnhanceOrSuppressFeatures'' module and ''IdentifyPrimaryObjects'' module contained in CellProfiler software. Segmentation masks of single cell and PI(3)P-positive structures, along with images of PI(3)P immunostaining were loaded in a custom MATLAB script. It assigned each PI(3)P-positive structure or pixel intensities to its corresponding cell and computed PI(3)P mean fluorescence intensity and counts. Mean fluorescence intensity was calculated by summing the pixel intensities of PI(3)P signal and dividing by the total number of pixels. A similar approach was used to quantify PI(3)P level in experiments designed to reduce PI(3)P, with the exception of single cell segmentation that as performed as follow. Single cells were automatically segmented using the signal of actin and nucleus staining. The nucleus was identified using DAPI and its boundaries were expanded to approximate the cell body. Actin was stained by CellMask Deep Red Actin (Invitrogen, A57245) and its signal was used to refine the segmentation, ensuring accurate delineation of the cell periphery. This procedure was implemented using ''IdentifyPrimaryObjects'' + ''IdentifySecondaryObjects'' modules contained in CellProfiler. These scripts were made available at Code Ocean: https://doi.org/10.24433/CO.3851388.v1.

Quantification of Rab stoichiometry in time lapse imaging (photon counting)

$5x10^4$ Cos-7 cells were plated in 8 well μ-Slide imaging dishes (Ibidi) and transfected with the indicated combination of fluorescent tagged version of biomolecular switches: EGFP-Rab5/mCherry-Rab11 or EGFP-Rab11/mCherry-Rab5. After 48 h, cells were starved for 2 h in serum-free DMEM 0.1% BSA at 37°C in 5% CO2. Human Transferrin (Invitrogen) was added at a concentration of 20 μg/ml for the time of the acquisition. Imaging was performed in a CO2 independent medium, Dulbecco's modified Eagle's medium without FBS. Cells were imaged using an inverted confocal Leica SP8 microscope with AOBS equipped with 63× O2/Oil immersion objective, NA 1.40. Acquisition was performed at zoom (×11) in a region of 26 μm in side. To obtain photon counting, the Hybrid Detector of LEICA SP8 microscope was set to ''Photon counting mode'' with 10-line accumulation. The number of measured photons was subsequently used to quantify absorbed switches on the endocytic structure.

Quantification of Rab activity and Loop Index using subsampled time-lapse experiments

Experimental abundances, activities and Loop IDXs were sampled from subregions of the ring-shaped ROI as follows. The ROI was split into 36 slices of 10° amplitude each. Then, the slice-wise mean activity was computed as the average FRET ratio intensity of

pixels composing the slice. The slice-wise Loop IDX (either $\rho(Rab5_{Mem}, Rab5^{GTP})$) or $\rho(Rab11_{Mem}, Rab11^{GTP})$) was quantified by computing the Pearson correlation between each GTPase's fluorescence and FRET ratio efficiency as reported in the equation in section "quantification of correlations from experimental data", where now *a* and *b* represent pixelwise intensities of the two signals, *i* corresponds to the pixel index (i.e., pixel spatial coordinates), and *n* indicates the total number of pixels contained in the slice.

Quantification of slice-wise mean activity and Loop IDX was performed for each time-lapse frame. We used mean activity and Loop IDX values obtained for each slice and each frame to compute their Pearson coefficient $c(Rab^{GTP}, Loop\ IDX)$ as follows:

$$c(FRET\ ratio, Loop\ IDX) = \frac{\sum_{i=1}^{n}(FRET\ ratio_i - \overline{FRET\ ratio})(Loop\ IDX_i - \overline{Loop\ IDX})}{\sqrt{\sum_{i=1}^{n}(FRET\ ratio_i - \overline{FRET\ ratio})^2}\sqrt{\sum_{i=1}^{n}(Loop\ IDX_i - \overline{Loop\ IDX})^2}}$$

The sampling of the endosome surface was visually represented by unrolling the sliced ring-shaped ROI on a vertical axis for each frame, to obtain kymographs representing the computed slice-wise mean abundances, mean activities, and Loop IDXs as functions of time.

Computation of Rab5 and Rab11 abundance and activity from experimental data

Mean Rab5 fluorescence, Rab11 fluorescence, Rab5 FRET ratio and Rab11 FRET ratio values were computed for each time-lapse frame within the entire ROI, using the previously processed images. Then, for each signal, its mean value inside the ROI was computed, and the so obtained frame-wise mean values were averaged over the entire time-lapse to compute global means for each series. Final mean fluorescence and FRET ratio values of control and Zfyve26 overexpression conditions were obtained by averaging results across time-lapses. *p* values were computed using t-tests. These scripts were made available at Code Ocean: https://doi.org/10.24433/CO.9194314.v1.

Computation of correlations from experimental data

The Pearson correlation between two distinct signals (e.g., mCherry-mVenus) was computed for the single frame as follows:

$$\rho(a,b) = \frac{\sum_{i=1}^{n}(a_i - \overline{a})(b_i - \overline{b})}{\sqrt{\sum_{i=1}^{n}(a_i - \overline{a})^2}\sqrt{\sum_{i=1}^{n}(b_i - \overline{b})^2}}$$

where *a* and *b* represent their pixelwise intensities, *i* identifies the pixel, and *n* indicates the total number of pixels contained in the ROI. Specifically, Pearson correlations involving the abundance and the active fraction of the same GTPase take the name of Loop IDX. The temporal dynamics of each Pearson correlation was obtained by computing it for each frame of a time-lapse. Then, the mean Pearson correlation for a single experiment was obtained by averaging Pearson correlation values. Final correlation values for control and Zfyve26 overexpression conditions were obtained by averaging results across time-lapses. *p* values were computed using t-tests. These scripts were made available at Code Ocean: https://doi.org/10.24433/CO.9194314.v1.

Computation of Rab5 and Rab11 abundances and activities in silico

In our theoretical framework, the total activity for each of the two GTPases is given by the sum of free active molecule and active molecule in complex with the effector:

$$[RabX^{GTP}] = [RabX^{GTP}_{Mem}] + [RabX^{GTP}_{Mem} : E]$$

$$[RabY^{GTP}] = [RabY^{GTP}_{Mem}] + [RabY^{GTP}_{Mem} : E]$$

Whereas the total membrane amount of each of the two GTPases is given by the sum of all their membrane-bound forms:

$$[RabX_{Mem}] = [RabX^{GDP}_{Mem}] + [RabX^{GTP}_{Mem}] + [RabX^{GDP}_{Mem} : E] + [RabX^{GTP}_{Mem} : E]$$

$$[RabY_{Mem}] = [RabY^{GDP}_{Mem}] + [RabY^{GTP}_{Mem}] + [RabY^{GDP}_{Mem} : E] + [RabY^{GTP}_{Mem} : E]$$

And the total amounts of the two GTPases are given by the sum of their cytoplasmic and membrane-bound forms:

$$[RabX_{Tot}] = [RabX^{GDP}_{Cyt}] + [RabX^{GDP}_{Mem}] + [RabX^{GTP}_{Mem}] + [RabX^{GDP}_{Mem} : E] + [RabX^{GTP}_{Mem} : E]$$

$$[RabY_{Tot}] = [RabY^{GDP}_{Cyt}] + [RabY^{GDP}_{Mem}] + [RabY^{GTP}_{Mem}] + [RabY^{GDP}_{Mem} : E] + [RabY^{GTP}_{Mem} : E]$$

Note that depending on the RabX (RabY) form hypothesized to interact with the effector, either of the terms $[RabX^{GDP}_{Mem} : E]$ or $[RabX^{GTP}_{Mem} : E]$ ($[RabY^{GDP}_{Mem} : E]$ or $[RabY^{GTP}_{Mem} : E]$) will be null in all such sums.

For each analyzed model, the corresponding ODE system was solved at the steady state for different stoichiometric conditions and variable values of parameters relative to effector-mediated control loops: equilibrium RabX and RabY membrane abundances ($RabX_{Mem}$, $RabY_{Mem}$) and activities ($RabX^{GTP}$, $RabY^{GTP}$) as functions of the effector amount were computed for fixed RabX, RabY total pool sizes ($RabX_{tot}$ = 200, $RabY_{tot}$ = 200), effector pool sizes ranging from 0 to 400 molecules, and maximum strengths of effector-mediated feedback/feedforward loops: depending on the loop sign acting on each GTPase, either its k_{GEFMAX} or its k_{GAPMAX} rate constant was varied, using values 10^0, 10^{-1},10^{-2}, 10^{-3}. Baseline values were maintained for the remaining parameters.

Equilibrium RabX and RabY membrane abundances ($RabX_{Mem}$, $RabY_{Mem}$) and activities ($RabX^{GTP}$, $RabY^{GTP}$) as functions of both effector and the RabX-RabY stoichiometric ratio were computed by simultaneously feeding the system with varying values of effector pool size (0–400 molecules) and $RabX_{tot}$/$RabY_{tot}$ ratio (10^{-1}-10^{1}), while keeping constant the total GTPase pool dimension ($RabX_{tot}$+$RabY_{tot}$ = 400 molecules). Baseline parameter values were used for computation.

Computation of correlations in silico

The Gillespie algorithm was used to compute correlations from simulated data of each model. Simulations were implemented within Julia programming language using the *Gillespie* package.[51,52] Then, simulated equilibrium abundances of each species were used to compute the Pearson correlation coefficient between molecule amounts of interest.

The Pearson correlation between distinct molecular species (e.g., $RabY_{Mem}$ and $RabX^{GTP}$) was computed as follows:

$$\rho(a,b) = \frac{\sum_{i=1}^{n}(a_i - \overline{a})(b_i - \overline{b})}{\sqrt{\sum_{i=1}^{n}(a_i - \overline{a})^2}\sqrt{\sum_{i=1}^{n}(b_i - \overline{b})^2}}$$

where a and b represent simulated equilibrium numbers of molecules of the two species, i identifies the specific simulation, and n indicates the total number of simulations.

In particular, correlations involving the membrane amount and the active amount of the same GTPase (i.e., $\rho(RabX_{Mem}, RabX^{GTP})$ and $\rho(RabY_{Mem}, RabY^{GTP})$ were named Loop IDXs.

All correlations, including Loop IDXs, for varying effector level were obtained by setting the effector pool dimension to values ranging from 0 to 400 molecules, maintaining fixed RabX and RabY pool sizes ($RabX_{Tot}$ = 200, $RabY_{Tot}$ = 200) and baseline parameter values. To add effector fluctuations, the value of effector was sampled from a Gaussian distribution with mean value corresponding to the pool size (0–400 molecules) and coefficient of variation CV = 0.05. After simulating the system for each mean effector pool dimension 10^4 times, we computed the Pearson correlation coefficient for a molecule pair over the 10^4 equilibrium values.

Pearson correlations between molecule pairs as functions of both effector and the Rab pool ratio were obtained by feeding the system with effector pool sizes ranging from 0 to 400 molecules and setting the Rab pool ratio $RabX_{Tot}$/$RabY_{Tot}$ to values from 10^{-1} to 10^{1}, maintaining the total GTPase pool size fixed ($RabX_{Tot}$+$RabY_{Tot}$ = 400 molecules). At each simulation with fixed effector pool size the E value was drawn from a Gaussian distribution centered at the corresponding mean value, with coefficient of variation CV = 0.05. Correlations were then calculated as the Pearson correlation coefficient of 10^4 steady-state simulation results.

Computation of Rab activity and Loop Index using subsampled in silico experiments

Sampling of activities and Loop IDXs with models C3 and C4 was performed as follows: 10^5 simulations with the Gillespie algorithm were realized using fixed baseline parameter values, equal amounts of RabX and RabY ($RabX_{tot}$ = 200 molecules and $RabY_{tot}$ = 200 molecules) and fixed effector amount (0, 50, 200, 400 molecules). Then, batches of 50 equilibrium molecule amounts were randomly drawn from the 10^5 fixed-effector results without repetition, thus obtaining 1000 batches. The batch-wise mean activity was computed by averaging Rab activity over the 50 values. Loop IDXs ($\rho(RabX_{Mem}, RabX^{GTP})$ and $\rho(RabY_{Mem}, RabY^{GTP})$) were computed for each batch as reported in the previous section (“quantification of correlations in silico”).

Thus, after obtaining both the average activity and the Loop IDX of a GTPase for each of the 1000 batches, the correlation between these two measurements was quantified by computing their Pearson coefficient as:

$$c\left(Rab^{GTP}, Loop\ IDX\right) = \frac{\sum_{i=1}^{n}\left(Rab^{GTP}{}_i - \overline{Rab^{GTP}}\right)\left(Loop\ IDX_i - \overline{Loop\ IDX}\right)}{\sqrt{\sum_{i=1}^{n}\left(Rab^{GTP}{}_i - \overline{Rab^{GTP}}\right)^2}\sqrt{\sum_{i=1}^{n}\left(Loop\ IDX_i - \overline{Loop\ IDX}\right)^2}}$$

Where Rab^{GTP} indicates any of the two Rab activities, either $RabX^{GTP}$ or $RabY^{GTP}$, *Loop IDX* represents correspondingly either $\rho(RabX_{Mem}, RabX^{GTP})$ or $\rho(RabY_{Mem}, RabY^{GTP})$, whereas i identifies the batch and n represents the total number of batches.

Statistical analysis of in silico and *in vitro* experiments

Statistical significance was determined by Kolmogorov-Smirnov test or Student's t test and indicated in the figure legend. The number of replicates is represented by n and is indicated in each figure legend. *$p < 0.05$; **$p < 0.01$; ***$p < 0.001$; ****$p < 0.0001$; ns, not significant unless otherwise stated in figure legend. Data are represented as mean ± SEM unless otherwise stated. Data analysis was preformed using GraphPad Prism (v9) and MATLAB (R2023a) software.